The Astrophysical Journal, 947:34 (19pp), 2023 April 10

New Velocity Measurements of NGC 5128 Globular Clusters Out to 130 kpc: Outer Halo Kinematics, Substructure, and Dynamics[*]

Allison K. Hughes[1] , David J. Sand[1] , Anil Seth[2] , Jay Strader[3] , Chris Lidman[4,5] , Karina Voggel[6] , Antoine Dumont[2] , Denija Crnojević[7] , Mario Mateo[8] , Nelson Caldwell[9] , Duncan A. Forbes[10] , Sarah Pearson[11,14] , Puragra Guhathakurta[12] , and Elisa Toloba[13]

[1] Steward Observatory, University of Arizona, 933 North Cherry Avenue, Tucson, AZ, 85721, USA; akhughes@email.arizona.edu
[2] Department of Physics & Astronomy, University of Utah, Salt Lake City, UT, 84112, USA
[3] Center for Data Intensive and Time Domain Astronomy, Department of Physics and Astronomy, Michigan State University, East Lansing, MI, 48824, USA
[4] Centre for Gravitational Astrophysics, College of Science, The Australian National University, ACT 2601, Australia
[5] The Research School of Astronomy and Astrophysics, Australian National University, ACT 2601, Australia
[6] Universite de Strasbourg, CNRS, Observatoire Astronomique de Strasbourg, UMR 7550, F-67000 Strasbourg, France
[7] University of Tampa, 401 West Kennedy Boulevard, Tampa, FL, 33606, USA
[8] Department of Astronomy, University of Michigan, Ann Arbor, MI, 48109, USA
[9] Center for Astrophysics, Harvard & Smithsonian, 60 Garden Street, Cambridge, MA, 02138, USA
[10] Centre for Astrophysics and Supercomputing, Swinburne University of Technology, Hawthorn VIC 3122, Australia
[11] Center for Cosmology and Particle Physics, Department of Physics, New York University, 726 Broadway, New York, NY, 10003, USA
[12] UCO/Lick Observatory, University of California Santa Cruz, 1156 High Street, Santa Cruz, CA, 95064, USA
[13] Department of Physics, University of the Pacific, 3601 Pacific Avenue, Stockton, CA, 95211, USA

Abstract

We present new radial velocity measurements from the Magellan and the Anglo-Australian Telescopes for 175 previously known and 121 newly confirmed globular clusters (GCs) around NGC 5128, the nearest accessible massive early-type galaxy at $D = 3.8$ Mpc. Remarkably, 28 of these newly confirmed GCs are at projected radii $>50'$ ($\gtrsim 54$ kpc), extending to ~ 130 kpc, in the outer halo where few GCs had been confirmed in previous work. We identify several subsets of GCs that spatially trace halo substructures that are visible in red giant branch star maps of the galaxy. In some cases, these subsets of GCs are kinematically cold, and may be directly associated with and originate from these specific stellar substructures. From a combined kinematic sample of 645 GCs, we see evidence for coherent rotation at all radii, with a higher rotation amplitude for the metal-rich GC subpopulation. Using the tracer mass estimator, we measure a total enclosed mass of $2.5 \pm 0.3 \times 10^{12}$ $M_\odot$ within ~ 120 kpc, an estimate that will be sharpened with forthcoming dynamical modeling. The combined power of stellar mapping and GC kinematics makes NGC 5128 an ongoing keystone for understanding galaxy assembly at mass scales inaccessible in the Local Group.

1. Introduction

Globular clusters (GCs), compact massive star clusters found in substantial numbers in all massive galaxies, provide a window into the various epochs of star formation that mark a galaxy's evolutionary history. In nearby galaxies ($D \lesssim 20$ Mpc), where detailed investigations with spectroscopy are possible, GC systems can provide important insights into the chemical and dynamical history of their hosts. Due to their high luminosities and compact sizes, GCs are observed much more easily than the underlying stellar field components in the remote parts of galaxies, allowing for efficient photometry and spectroscopy. Various studies have found correlations between GC systems and their host galaxy properties that can shed light on galaxy formation

mechanisms (Brodie & Strader 2006). GC kinematics provide information about the assembly history of the host galaxy, its total mass, and its dark matter distribution (e.g., Schuberth et al. 2010; Strader et al. 2011; Schuberth et al. 2012; Alabi et al. 2017). GCs also provide an alternative way to look for and study past accretion events, by searching for spatially and dynamically linked GC groups that can serve as tracer populations for their (now disrupted) parent systems (e.g., Mackey et al. 2010; Veljanoski et al. 2014; Kirihara et al. 2017; Mackey et al. 2019).

The most numerous populations of GCs are found in luminous elliptical galaxies, especially those at the center of massive groups or clusters (Harris & Racine 1979; Brodie & Strader 2006; Richtler 2006), which can have thousands of GCs. However, there are still only a handful of galaxies that have a large population ($\gtrsim 500$) of GCs with measured radial velocities, including the cluster-central galaxies M87 (Côté et al. 2001; Strader et al. 2011; Zhang et al. 2015; Forbes et al. 2017) and NGC 1399 (Richtler et al. 2004; Schuberth et al. 2010; Pota et al. 2018). These large samples of velocities are necessary to move beyond rough halo mass estimates to measurements of the halo concentration, searches for substructure, and constraints on the ongoing assembly of the

dynamically young outer regions of the halo (e.g., Romanowsky et al. 2012; Chaturvedi et al. 2022).

Historically, NGC 5128 (Centaurus A) has been a leading target for extragalactic GC studies due to its proximity and the richness of its GC system. NGC 5128 is the central elliptical galaxy in a group of galaxies at a distance of 3.8 ± 0.1 Mpc (Harris et al. 2010). Since the first discovery of GCs in NGC 5128 in the 1980s, many photometric and spectroscopic surveys have been conducted, leading to the identification of ~600 confirmed GCs and thousands of GC candidates (Graham & Phillips 1980; van den Bergh et al. 1981; Harris et al. 1984; Hesser et al. 1984, 1986; Harris et al. 1992; Minniti et al. 1996; Alonso & Minniti 1997; Holland et al. 1999; Rejkuba 2001; Harris et al. 2002; Peng et al. 2004a; Harris et al. 2004; Martini & Ho 2004; Woodley et al. 2005; Gómez et al. 2006; Harris et al. 2006; Gómez & Woodley 2007; Rejkuba et al. 2007; Woodley et al. 2007; Beasley et al. 2008; McLaughlin et al. 2008; Georgiev et al. 2009; Woodley et al. 2010a, 2010b; Georgiev et al. 2010; Mouhcine et al. 2010; Sinnott et al. 2010; Taylor et al. 2010; Harris et al. 2012; Taylor et al. 2015, 2017; Fahrion et al. 2020; Voggel et al. 2020; Müller et al. 2021; Dumont et al. 2022), some of which are associated with nearby dwarf galaxies. Besides the identification of GCs through photometry and spectroscopy, there have also been searches cross-matched with X-ray observations (e.g., Minniti et al. 2004; Jordán et al. 2007; Woodley et al. 2008). While the bulk of the stellar mass in NGC 5128 is that of an old metal-rich massive elliptical galaxy, the galaxy also shows a peculiar shape and recent star formation that point to a relatively recent gas-rich merger, as well as numerous halo substructures that point to an ongoing active accretion history (e.g., Baade & Minkowski 1954; Graham 1979; Israel 1998; Mould et al. 2000; Rejkuba 2001; Peng et al. 2002; Rejkuba et al. 2002; Crockett et al. 2012; Crnojević et al. 2016; Wang et al. 2020).

The goal of the present study is to improve our understanding of the outer halo of NGC 5128 via a newly enlarged, updated sample of radial-velocity-confirmed GCs. We combine these GC velocities with a wide-field resolved red giant branch (RGB) star map of the galaxy out to a projected galactocentric radius of ~150 kpc produced by the Panoramic Imaging Survey of Centaurus and Sculptor (PISCeS; Crnojević et al. 2016), allowing matches between outer halo GCs and specific stellar substructures. We show that we can successfully apply this method of tracing individual galactic accretion signatures with GCs to NGC 5128, which had previously only been used on a large scale inside the Local Group (e.g., Veljanoski et al. 2014).

This paper is organized as follows. Section 2 describes our observations and data reduction process for the optical spectroscopy from Magellan/M2FS and Anglo-Australian Telescope (AAT)/AAOmega. In Section 3 we discuss our methodology for measuring radial velocities and present our sample of radial velocity measurements for previously known and newly confirmed GCs in NGC 5128. We analyze the updated GC population in Section 4. In Section 5 we identify GCs belonging to specific substructures within the halo of NGC 5128, and estimate a mass profile for the galaxy in Section 6. We summarize and conclude in Section 7.

As in our previous GC work around NGC 5128 in Hughes et al. (2021), hereafter H21, we adopt a distance modulus for NGC 5128 of $(m - M)_0 = 27.91$ mag, corresponding to a distance of $D = 3.82$ Mpc (Harris et al. 2010). The physical scale at this distance is 18.5 pc arcsec^{-1} (1.1 kpc arcmin^{-1}).

2. Observations and Data Reduction

In this section, we first summarize our GC candidate selection technique, underpinned by our work presented in H21. Following this, we present our new Magellan/M2FS and AAT/AAOmega optical spectroscopy to identify new radial-velocity-confirmed GCs in the NGC 5128 system out to large radii.

2.1. GC Candidate Selection

H21 focused on GC selection out to a projected radius of ~150 kpc from the galaxy center using the 95 PISCeS fields (Crnojević et al. 2016, 2019). Each PISCeS field has an ~24'×24' field of view with a binned (2×2) scale of 0″16 per pixel and a median of 0″65 seeing in the g and r bands. To summarize the steps of the GC candidate selection process: (i) using the newly derived photometry, we first made a selection in magnitude, excluding both the brightest GC candidates ($r \lesssim 18$ mag, affected by saturation) and faintest ones ($r \gtrsim 22$ mag, beyond which ancillary data are mostly missing and contamination is substantial), as well as those GCs affected by crowding near the galaxy's center ($<10'$ from NGC 5128); (ii) we did a likelihood-based selection of extended objects likely to be GCs using a two-aperture technique on the PISCeS photometry, measured by the concentration index C_{3-6} (the difference in magnitude between three and six pixel apertures); (iii) we rejected background galaxies and stellar blends using cuts in the effective radius, ellipticity, and large-radius flux distribution; (iv) we added data from Gaia DR2 to reject foreground stars using measurements of astrometric motion (proper motion and parallax) and proxies for extendedness (astrometric excess noise and BP/RP excess), as GCs at the distance of NGC 5128are slightly resolved; and (v) we used multiband photometry from the NOAO Source Catalog (NSC) to assign a likelihood that each source has colors consistent with known GCs (Nidever et al. 2018). For each step a quantitative likelihood was assigned, and a final *total_likelihood* for each candidate was calculated by multiplying each of these likelihoods together (with no penalty when data were missing). Numbers closer to unity represent a larger chance that the source is a GC associated with NGC 5128. Again, we refer the reader to H21 for details.

Based on the amount of data available, each GC was also placed into one of four categories: gold if the GC had data in PISCeS, Gaia DR2, and NSC; (2) silver if the GC had data in PISCeS and one of Gaia DR2 or NSC; (3) bronze if the GC had data only in PISCeS and was well resolved with $C_{3-6} > 2.0$; and (4) copper if the GC had data only in PISCeS and was marginally resolved with $2.0 > C_{3-6} > 1.0$. We identified a total of 40,502 GC candidates, the vast majority of which are likely contaminants. Of these, we highlighted the 1931 gold and silver candidates with *total_likelihood* > 0.85 as the highest priority for spectroscopic follow up for confirmation (see Table 3 in H21 for a breakdown of the number of GC candidates in each data rank).

The GC candidate selection process described above was designed for GCs in the magnitude range $18 \lesssim r \lesssim 22$ mag, and does not include either very bright or very faint GCs. For bright GCs, our team used a parallel effort to identify bright GCs/

Table 1
M2FS Observation Summary

| Field | UT Date | Field Center | | Time | Exposures | Typical |
		R.A. (J2000)	Decl. (J2000)	(hr)		Seeing
1	2017 Feb 25	13:25:41.1	−43:22:13	3.0	4	1″.1
2	2017 May 21	13:23:53.0	−42:59:41	3.0	4	0″.8
3	2017 May 21	13:28:11.4	−43:21:34	3.0	4	0″.8
4	2017 June 4	13:24:07.6	−42:35:50	3.2	4	0″.9
5	2018 May 12	13:30:31.1	−42:03:14	2.5	3	0″.7
6	2019 Feb 27	13:25:10.3	−42:56:29	3.3	5	0″.9
7	2019 March 7	13:26:51.9	−42:39:16	1.5	3	0″.9
8	2019 March 5	13:24:53.8	−43:27:51	1.75	3	1″.5
	2019 June 2			1.5	3	0″.8

ultracompact dwarfs ($L_V \geqslant 2 \times 10^5 L_\odot$, roughly corresponding to $M \geqslant 3 \times 10^5 M_\odot$) out to similarly large radii (~150 kpc; Voggel et al. 2020; Dumont et al. 2022). Also, beyond the conservative color selection described above, we did not further prioritize between red and blue GC candidates, and so there should be no preferential selection of metal-rich versus metal-poor GCs. Hence this process should lead to a minimally biased sample of candidate GCs with $r \lesssim 22$ in NGC 5128. No matter the selection method, we also include all known, radial-velocity-confirmed GCs in our kinematic analyses in the later sections of this work.

The optical spectroscopy detailed below was taken over five years, with some of the earliest data obtained before our final rigorous likelihood-based target selection was in place and hence based on preliminary photometry with less ancillary data. We evaluate the in-practice success of our selection methods in Section 3.4.

2.2. Magellan/M2FS

We obtained multiobject fiber spectroscopy using the Michigan/Magellan Fiber System (M2FS) instrument on the Magellan/Clay 6.5 m telescope at the Las Campanas Observatory on several runs between 2017 and 2019. The M2FS Spectrograph consists of twin spectrographs, each of which can be fed by up to 128 1″.2 diameter fibers over a field of view 30′ in diameter (Mateo et al. 2012). The twin spectrographs can be set to different resolution modes, and we used this to accomplish two science goals simultaneously. The "high" resolution echelle mode was used to measure stellar velocity dispersions of bright GSs and ultracompact dwarfs to identify stripped galaxy nuclei that might contain massive central black holes, as discussed in Dumont et al. (2022). In the current work, we used the "low" resolution data obtained from the other spectrograph, with a resolution of $R \sim 1300$ and wavelength range 4100–6000 Å, to measure radial velocities and confirm the nature of the GC candidates from H21. We focused on radial velocity measurements using the strong Hβ (4861 Å) and magnesium triplet (Mg b, 5167–5183 Å) absorption features.

Owing to the relatively smaller field of view of M2FS compared to AAOmega, we generally observed fields closer to the central regions of NGC 5128 due to the higher density of good GC candidates at these projected radii. The exception is pointing 5, which was positioned to capture CenA-Dw1 and CenA-Dw3, two important stellar substructures discussed further in Section 5. Within each field we prioritized candidates based on preliminary versions of our H21 cluster catalog.
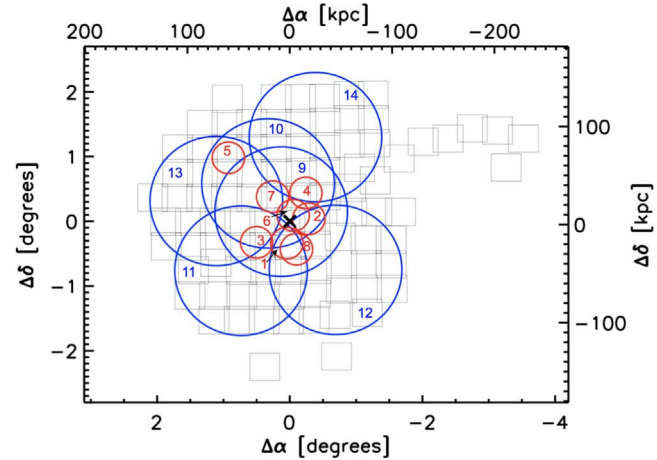

Figure 1. Footprint of the PISCeS survey (small pale squares) around NGC 5128, oriented such that north is up and east is left. The center of NGC 5128, located at $\alpha = 201°.362540$, $\delta = -43°.033627$, is marked by the central black "x." Regions observed with Magellan/M2FS are indicated by the red circles and those observed with AAT/AAOmega are indicated by the blue circles, with positions given in Tables 1 and 2.

Across the eight M2FS fields, we measured spectra for 750 unique targets. Some of these targets were measured in multiple fields, and we also intentionally reobserved some velocity-confirmed GCs to test the fidelity of our velocity measurements, as discussed in Section 3.

Table 1 lists the date, field center location in R.A. and decl. in J2000 coordinates, total exposure time, number of exposures, and typical seeing for each field. Figure 1 illustrates the M2FS field center positions with respect to NGC 5128 and the PISCeS data set (along with our AAOmega fields). Typically, each field was observed over the course of one night, though Field 8 was split over two observing runs in 2019. The data from the two observing runs were treated separately, and independent velocity measurements were extracted from each. The Field 7 exposure time is lower than for the other fields due to a technical issue that occurred with the telescope during observing.

The M2FS observations are made in queue mode, and observing blocks are typically scheduled in dark or gray time. All of the data were taken in relatively clear skies with ~0″.7–1″.5 seeing. Individual exposures of typically 45 minutes were combined into the final spectra. In addition to science images, we also took a set of calibration frames in the afternoon or during the night, including twilight flats, biases,

Table 2
AAOmega Observation Summary

Field	UT Date	Field Center		Time (hr)	Exposures	Typical Seeing
		R.A. (J2000)	Decl. (J2000)			
9	2017 May 4	13:26:09	−42:53:02	4.5	10	1″6
10	2017 May 5	13:27:14	−42:26:54	6.5	13	1″5
11	2019 March 30	13:29:28	−43:47:49	2.0	4	3″0
12	2019 March 30	13:21:40	−43:46:58	2.5	5	3″5
13	2022 April 23	13:31:30	−42:43:09	4.0	8	1″8
14	2022 May 5	13:23:19	−41:44:00	6.5	13	2″0

darks, thorium argon (ThAr) wavelength calibration arcs, and fiber maps.

Data reduction was performed using standard IRAF (Tody 1986) routines, as discussed in Walker et al. (2015). First, we applied an overscan correction and trimmed each raw image, and applied zero level and dark count corrections. Cosmic rays were also identified and interpolated over using L. A. Cosmic (van Dokkum 2001). Individual science exposures were combined into a single, stacked science frame. We calculated the scattered light in each image by fitting a surface function to the area between the fibers and subtracted this from the stacked science frames. Then we traced fiber positions using twilight flat images, and extracted 1D spectra. We performed wavelength calibration using ThArNe or ThAr 1D lamp spectra. Each M2FS field had between 12 and 20 fibers pointed at empty sky, which were averaged together and subtracted from the science spectra. We used the resulting science spectra and associated variance spectra to measure radial velocities.

2.3. AAT/AAOmega

We obtained additional multiobject fiber spectroscopy using the 2dF/AAOmega instrument on the AAT 3.9 m telescope at the Siding Springs Observatory in Australia in 2017, 2019, and 2022. 2dF is a multiobject fiber feed to the dual-arm AAOmega spectrograph that is designed to allow the acquisition of up to 400 simultaneous spectra of objects across a two degree field on the sky (Sharp et al. 2006). For the blue arm, we used the 580V grating, corresponding to a resolution of $R \sim 1300$, and a wavelength range of ≈ 3500–5500 Å to cover the Hβ and Mg b lines. For the red arm, we used the 1000I grating, corresponding to a resolution of $R \sim 4400$, and a wavelength range of ≈ 8200–9300 Å to cover the calcium triplet (Ca) lines. Our observing program was designed with the red arm in mind, but we use the blue arm spectra as a useful cross-check. The projected fiber diameters vary between 2″0 and 2″1 across the field of view.

Due to its very wide field, we used 2dF/AAOmega to cover the outer regions of NGC 5128. Table 2 lists the date, field center location in R.A. and decl. in J2000 coordinates, total exposure time, number of exposures, and typical seeing for each field. Figure 1 shows the relative positions for each field. Seeing ranged from 1″4 to 4″0 on the different observing nights, and we made adjustments to the exposures times to partially account for these variations. All individual exposures were 30 minutes.

We prioritized GC candidates with higher *total_likelihood* values from our selection process, although in 2017 and 2019 the selection methodology of H21 was not yet finalized. In addition to science images, we also took arcs, flats, and bias

images. Across the six AAT fields, we measured velocities for 1780 unique targets. Similar to our procedure with M2FS, we intentionally observed some GC candidates in multiple fields and reobserved confirmed GCs to test the fidelity of our velocity measurements.

We used 2DFDR, the data reduction package for AAOmega, to reduce our spectroscopic data.[15] We extracted light from the fibers with optimal extraction and used a third-order polynomial for the wavelength solution. For the red arm, the relative intensities of the sky lines in the object data frames were used to determine the relative fiber throughput, using the SKYLINE(KGB) algorithm within 2DFDR. Because the wavelength range of the blue arm had few bright sky lines, we instead adopted the fiber-to-fiber normalization values from the red arm. The final product of 2DFDR used in this paper was the combined spectrum of each target and an associated variance array.

3. Radial Velocities

In this section, we discuss our methodology for measuring radial velocities for our spectroscopic sample. Following this, we compare our measurements with existing GC radial velocity measurements in the literature, and present our sample of newly confirmed GCs in NGC 5128. With these results in hand, we evaluate our GC candidate selection technique reported in H21.

3.1. Measuring Radial Velocities

We use similar procedures for measuring radial velocities in both our M2FS and AAOmega data sets, employing a cross-correlation procedure over different wavelength ranges. We ensure robust velocities by cross-checking our results between these different wavelength ranges, along with visual inspection of individual velocity measurements.

We computed radial velocities for our spectra via Fourier cross-correlation, using `fxcor` in IRAF. For the bluer data (M2FS and blue AAOmega data), we used a composite spectrum of M31 GCs (with a signal-to-noise ratio of S/N > 500) as a template (Caldwell et al. 2011). We cross-correlated this around the Hβ and Mg b spectral lines over the wavelength windows shown in Figure 2, noting that the latter region also includes Fe lines that can also be strong in metal-rich GCs. We compared the results using this composite template both to those obtained by using candidate template stars of various spectral types obtained with the same instrument and also to synthetic model spectra, and found that the M31 composite best reproduced existing high-precision
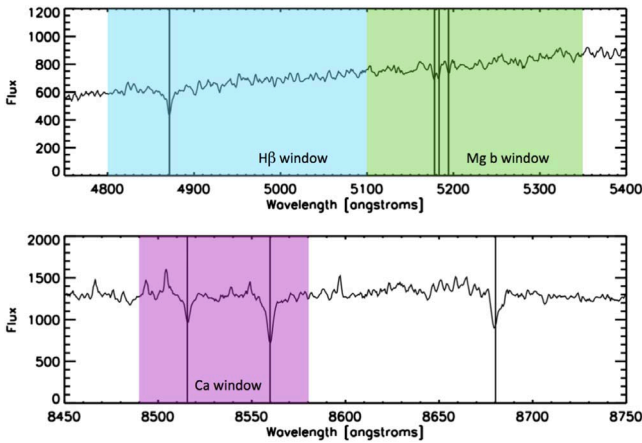
---

[15] https://aat.anu.edu.au/science/software/2dfdr

Figure 2. Wavelength windows used to compute radial velocities via Fourier cross-correlation in fxcor in IRAF. In this example, we measure the target to have a radial velocity of 620 km s^{-1}. For AAOmega, all displayed regions are used; for the M2FS observations, only the Hβ and Mg b triplet windows are used due to our wavelength coverage.

velocities with fidelity. The comparison between our results and known velocities is discussed in Section 3.2. Lacking a comparable template in the red Ca triplet region, we instead used a template based on the twilight solar spectrum. All velocities were corrected to the barycentric frame.

A well-known challenge to determining radial velocities via cross-correlation is the possibility of a "catastrophic" mis-identification of the principal cross-correlation peak, which is a particular problem for low-S/N spectra, especially when the noise is nonGaussian as can arise from poorly subtracted sky lines. To address this potential issue, we require consistent cross-correlation results between at least two spectral features, and we also visually checked the candidate velocities for all spectra. In total, we measure accurate velocities for a total of 964 objects. For the M2FS data that resulted in a velocity measurement, we calculated a median S/N (per pixel) of 12.9 (14.5) and an R value of 20.5 (26.9) for the Hβ (Mg b triplet) feature, while for the AAOmega data we have a median S/Ns (per pixel) of 10.3, 10.5, and 17.7 and R values of 19.6, 23.3, and 28.6 for the Hβ, Mg b triplet, and Ca triplet, respectively. In all cases, the minimum S/N for which a successful velocity was measured was S/N $\approx$ 3–3.5. Here the R value is a measure of the cross-correlation peak height with respect to the rest of the cross-correlation function (Tonry & Davis 1979), and is a standard output of the fxcor routine.

Regarding uncertainties, for the M2FS data we have a sufficient number of repeat observations between different fields to allow for an estimate of the velocity uncertainties as a function of S/N. Following the procedure in Kimmig et al. (2015), we calculated the velocity differences between pairs of spectra that both passed our quality criteria. We then binned these pairs in S/N, and calculated the spread of the paired velocity differences within each bin (using the median absolute deviation as a robust measure of the spread). Finally, we fit a relation between the S/N and this measure of the spread. We use this relation to assign an uncertainty to each velocity based on the S/N of the parent spectrum, where the uncertainty is related to this spread by a factor close to unity (see Kimmig et al. 2015 for additional discussion). On the basis of existing GC radial velocity studies at similarly low spectral resolutions and comparable S/Ns (e.g., Strader et al. 2011), we set a

minimum radial velocity uncertainty of 10 km s^{-1} for the M2FS and AAOmega velocities.

Because we did not have many targets that were observed in more than one AAOmega field, we estimated uncertainties using a similar methodology, but applied it instead to the velocities measured separately from the blue and red arm spectra. We fit a power law to the binned median difference in radial velocity measurements between the blue and red arms as a function of S/N. The error assigned to a given spectrum is based on its S/N and the power-law fit to these median values, with a floor uncertainty of 10 km s^{-1} for all of our measurements.

The final reported M2FS and AAOmega heliocentric radial velocity measurements are weighted averages of the respective velocity measurements (see the windows in Figure 2) that passed visual confirmation. Our radial velocity values for the previously confirmed GCs in the literature are consistent within our measured uncertainties, as discussed in the next section.

3.2. Literature Comparison

During our observations with M2FS and AAOmega we intentionally observed previously confirmed GCs to test the fidelity of our velocity measurements and to reduce the uncertainties associated with the velocities of the confirmed GCs. We use the catalog of confirmed GCs from Woodley et al. (2010a), hereafter W10, as reference because they are the most recent survey to publish a large sample of composite velocity measurements. We obtained new radial velocities for 108 confirmed GCs from the W10 catalog. In Figure 3 we show a comparison of our measured velocities with the weighted velocities from W10. Overall, the measurements agree very well, with a median difference of -3 ± 3 km s^{-1} (1 ± 7 km s^{-1}) between the AAT (M2FS) data and W10, where the uncertainty is a robust rank-based estimate of the standard deviation divided by the square root of the number of measurements.

While W10 was the largest single previous compilation of velocities, other subsequent studies contributed additional data, and overall there are 175 previously confirmed GCs with radial velocities that we reobserved. Table 3 lists the GC IDs from H21 or the present work, the R.A. and decl. in J2000 coordinates, the PISCeS g and r magnitudes, the PISCeS $(g - r)_0$ and NSC $(u - z)_0$ colors with a Milky Way dust correction applied on a source-by-source basis (Schlafly & Finkbeiner 2011), and the new velocity measurements from M2FS and AAOmega. It also lists the *new* weighted velocity measurements combining new measurements from the current work and all previous velocity measurements used in the weighting, as listed in the final column. The astrometry listed is primarily from PISCeS (see H21), but not in all cases, since some sources are outside of the usable PISCeS area or are saturated. Hence, the astrometry listed is not homogeneous, but should be of sufficient precision to identify all sources unambiguously.

Among these repeats, there are only a few cases of greatly differing velocity measurements between the current survey and the literature (see Figure 3). We discuss each of these in detail in the Appendix, along with a handful of conflicting measurements in the literature which we were able to resolve with our new spectroscopic data.

Because of the high rate of foreground star contamination among GC candidates with velocities <250 km s^{-1} (see the
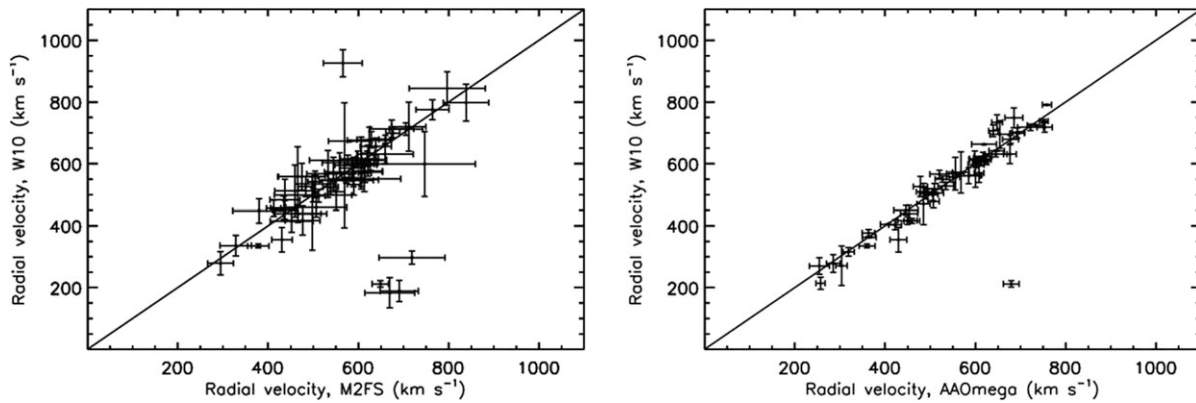
Figure 3. We compare the radial velocities measured from M2FS (left) and AAOmega (right) to the weighted radial velocity measurements in the W10 catalogs, showing that with a small number of exceptions our velocities agree with the published velocities with high fidelity. The 1:1 line is shown. The outlying, inconsistent sources are discussed in detail in Appendix A.1; these include those sources in the lower right of each plot, and the single point in the upper regions of the left M2FS comparison plot.

discussion below), we only include GCs in our final catalog of confirmed objects if their radial velocities are >250 km s⁻¹ or if they are clearly resolved in high-resolution imaging from the Hubble Space Telescope.

3.3. Newly Confirmed GCs

NGC 5128 has a systemic velocity of 541 km s⁻¹ (Hui et al. 1995), and a central stellar velocity dispersion of ∼150 km s⁻¹ (Wilkinson et al. 1986). Therefore, to avoid contamination from Milky Way foreground stars, past surveys have generally considered a GC to be confirmed if its radial velocity is ≳250 km s⁻¹, at about 2σ below systemic. Some studies have confirmed GCs at lower velocities, or without a velocity measurement at all, based instead on structural parameters (for example, being resolved in ground-based or space-based imaging).

For our new data, we classify candidates as GCs if they have radial velocities greater than 250 km s⁻¹ and lack contravening evidence (i.e., a significant proper motion). Below this limit, we considered objects as potential GCs on a case-by-case basis, though we ultimately did not find indisputable evidence for additional GCs in this velocity range in our new data. This is not too surprising given that perhaps ∼2% of our sample might be expected to have such low velocities. Our ability to separate foreground stars from low-velocity GCs with confidence is substantially improved compared to most previous work on NGC 5128 given the availability of Gaia, which allows the rejection of foreground stars as objects with significant proper motions that might otherwise be classified as potential GCs.

We find a total of 121 new NGC 5128 GCs based on our radial velocity measurements. Table 4 lists the IDs from H21 or here, the R.A. and decl. in J2000 coordinates (with the same caveats on the astrometry as for Table 3), the PISCeS g and r magnitudes not corrected for dust, the PISCeS $(g − r)_0$ and NSC $(u − z)_0$ colors with a Milky Way dust correction applied on a source-by-source basis (Schlafly & Finkbeiner 2011), and the measured radial velocities from M2FS and AAOmega.

As a final check for both our new GC candidates and for those with only radial velocity measurements from the literature, we cross-match all candidate GCs against Gaia DR3 (Gaia Collaboration et al. 2022) to see if they have

measured proper motions or parallaxes that could suggest a foreground star classification (recall that our GC selection technique used for spectroscopic targeting employed Gaia DR2). Any candidates with high-significance (5σ) Gaia DR3 proper motions and radial velocities <250 km s⁻¹ are classified as stars. For a few objects the evidence is mixed: these cases are discussed in more detail in the Appendix. Not all targets have Gaia data, so this evaluation is partially incomplete, but it still represents a meaningful advance in the purity of the final GC sample.

We plot the positions of all confirmed GCs with radial velocities in Figure 4. We discovered 28 new GCs at large radii, at >50′ (≈54 kpc), with the most distant new object at a radius of 122′ (≈130 kpc). These newly confirmed distant GCs are primarily to the north of the galaxy, though we emphasize that this region also benefited from the finalized GC candidate selection technique and received the most amount of observing time. An additional 69 new GCs are within 30′ (≈32 kpc), which illustrates that substantial scope exists for confirmation of more centrally located candidates as well.

As a resource for future follow-up observations, we also include a table of 656 stars and 12 galaxies identified via radial velocity measurements from M2FS and AAOmega in Table 5.

3.4. Evaluation of the GC Selection Technique

In H21, we highlighted GC candidates of gold and silver rank with a *total_likelihood* ⩾ 0.85 as the most likely to be true GCs in NGC 5128 and therefore the most promising targets for follow-up spectroscopic confirmation. We refer to this combined sample here as the "priority" sample. Because our spectroscopic observations were taken over a few years while we were still refining our techniques, our GC candidate selection process changed between observation runs. This means that the earlier spectroscopic observations were more likely to include contaminating foreground stars and background galaxies.

We observed 655 of the H21 priority sample targets during our observing runs with Magellan/M2FS and AAT/AAOmega. Of these, 179 (27%) are found to be new or previously confirmed GCs and 134 (20%) are found to be foreground stars or background galaxies. The remainder could not be conclusively identified, typically due to low S/Ns. Of those GC

Table 3
Radial Velocity Measurements of Previously Known GCs in NGC 5128

H21/22-ID	R.A. (deg J2000)	Decl. (deg J2000)	g (mag)	r (mag)	$(g-r)_0$ (mag)	$(u-z)_0$ (mag)	M2FS v_r (km s^{-1})	AAOmega v_r (km s^{-1})	Weighted v_r (km s^{-1})	Notes
H21-155942	200.50859	−42.53533	18.95	18.25	0.54	2.14	⋯	643 ± 10	639 ± 2	12
H21-194226	200.90970	−42.77302	18.86	18.22	0.49	1.99	⋯	479 ± 26	486 ± 20	7
H21-195812	200.92642	−43.16045	19.37	18.64	0.59	2.36	⋯	374 ± 17	379 ± 15	4,7
H21-196535	200.93407	−43.18659	18.12	17.38	0.74	⋯	...	647 ± 17	648 ± 6	1,2,4,7,9,10
H21-196891	200.93760	−43.01983	19.67	18.85	0.69	2.77	589 ± 14	⋯	581 ± 13	9
H21-198648	200.95671	−43.24220	19.38	18.55	0.68	2.71	⋯	675 ± 17	682 ± 15	4,7
H21-200443	200.97577	−43.36572	22.67	21.65	1.01	⋯	459 ± 44	⋯	470 ± 39	9

Note. The complete table will be available online. Radial velocities measured by: 1 = van den Bergh et al. (1981); 2 = Hesser et al. (1986); 3 = Harris et al. (1992); 4 = Peng et al. (2004a); 5 = Woodley et al. (2005); 6 = Rejkuba et al. (2007); 7 = Beasley et al. (2008); 8 = Woodley et al. (2010b); 9 = W10; 10 = Taylor et al. (2010); 11 = Voggel et al. (2020); and 12 = Dumont et al. (2022).

(This table is available in its entirety in machine-readable form.)

candidates not in the priority sample, only 7% are found to be new or previously confirmed GCs.

We expect the level of contamination to be higher in the outer regions of the galaxy where the density of GCs is lower. Dividing the sample at 30′ (33 kpc), we find that within this radius, the fraction of confirmed GCs is 143 out of 209 (68%), while beyond 30′, we confirm 36 out of 446 (8%).

4. Analysis of the Updated GC Population

In this section we look at the 2D and radial distributions of the updated confirmed GC population as a whole, as well as split into metal-poor and metal-rich subpopulations. We identify GCs associated with stellar substructures seen in the RGB star map from the PISCeS survey. Lastly, we look at the distribution of radial velocities and calculate an updated mean value and velocity dispersion for the GC system.

After our new measurements and analysis of literature objects in Section 3.3, the full sample of confirmed GCs with radial velocity measurements in NGC 5128 is now 645. This number includes the 121 new measurements presented here. We plot the positions of these radial-velocity-confirmed GCs around NGC 5128 in Figure 4. While 88% of the total confirmed GC population is within 30′, there are many GCs out to ≈100′ (≈108 kpc), with the farthest known GC at a projected radial distance of 173′ (187 kpc).

4.1. Surface Density and Metallicity Trends

Given the clear observed bimodal color distribution of GCs in NGC 5128 (Figure 5), we make the usual subdivision of the GCs into either metal-poor (blue) or metal-rich (red) subpopulations based on their NSC colors. We use the same divide as in H21, such that GCs with $(u-z)_0 < 2.6$ are in the metal-poor sample and GCs with $(u-z)_0 > 2.6$ are in the metal-rich sample. For those GCs that do not have photometry in NSC, we find an equivalent divide at $(g-r)_0 = 0.65$ based on the PISCeS photometry, as shown in Figure 5 (where GCs can appear in both the top and bottom panels). There are nine GCs with radial velocity measurements that do not have photometry in either the NSC or the PISCeS catalog, and as such they are not included in the subsequent color-based subpopulation analysis. Most of these GCs without photometry are within 5′ of the galaxy center, where ground-based photometry is difficult due to the extremely high and variable background of NGC 5128's central regions. We emphasize that beyond our conservative overall color

selection of GC candidates (see H21), we did not preferentially follow up blue or red GC candidates.

We find that 55% of the confirmed GCs are metal poor and the other 45% are metal rich. Within ∼10′, there are approximately equal numbers of metal-poor and metal-rich GCs. Beyond this, metal-poor GCs begin to dominate. The radial distributions of the velocity-confirmed GCs with $20.5 > r > 17.5$ are plotted in Figure 6, where we have imposed the faint magnitude limit to ensure there is no bias between the M2FS and AAOmega samples, and the bright limit to guard against the possibility that stripped nuclei (Dumont et al. 2022) could affect our results. These plotted surface densities are calculated in circular annuli with near-constant numbers of GCs.

As discussed above, the GC sampling is incomplete in the inner regions of the galaxy. We find that over a radial range of 7′–30′, power laws appear to provide excellent fits to the surface density of the total sample, as well as the blue and red subpopulations. The best-fit power-law indices for the total, blue, and red subpopulations are -2.69 ± 0.19, -2.64 ± 0.27, and -3.05 ± 0.28, respectively, and these fits are plotted in Figure 6. The uncertainties in these fits are derived from bootstrapping (resampling with replacement). These power-law values for the surface density profile are converted to physical 3D density profile indices of 3.69 ± 0.19, 3.64 ± 0.27, and 4.05 ± 0.28, respectively, for use in Section 6 and our mass estimates.

The metal-rich subpopulation has a slightly steeper slope and is more centrally concentrated than the metal-poor subpopulation, which follows trends observed in other extragalactic GCs studies (e.g., Brodie & Strader 2006; Faifer et al. 2011; Forbes et al. 2012).

At the largest radii covered by these data, the spatial distribution of the GCs is no longer smooth. As discussed further in Section 5, GCs associated with stellar substructures in the outer halo of NGC 5128 make up a substantial fraction (at least a third, and possibly more) of the GCs beyond ∼50′. The vast majority of the GCs associated with visible substructures are metal poor, consistent with the ongoing assembly of the metal-poor outer halo of NGC 5128.

4.2. Radial Velocity Distributions

Radial velocity histograms are shown in Figure 7 for the entire confirmed GC system, as well as the subpopulations of

Table 4
Radial Velocity Measurements of the Newly Confirmed GCs in NGC 5128

H21/H22-ID	R.A. (deg J2000)	Decl. (deg J2000)	g (mag)	r (mag)	$(g - r)_0$ (mag)	$(u - z)_0$ (mag)	M2FS v_r (km s^{-1})	AAOmega v_r (km s^{-1})
H21-082748	199.70710	−43.49976	19.94	19.41	0.37	1.56	⋯	300 ± 18
H21-115063	200.10130	−43.56268	19.61	18.81	0.65	2.40	⋯	257 ± 13
H21-144922	200.39422	−43.51873	19.26	18.60	0.51	2.01	⋯	513 ± 17
H21-155829	200.50759	−43.43897	20.42	19.45	0.81	2.82	⋯	536 ± 22
H21-166444	200.61574	−41.74595	21.49	20.20	1.17	3.33	⋯	269 ± 14
H21-166516	200.61649	−42.08955	21.11	20.28	0.69	2.22	⋯	275 ± 14
H21-184891	200.80609	−43.83047	19.34	18.63	0.56	2.21	⋯	502 ± 15
H21-186688	200.82601	−43.03390	20.61	19.89	0.57	2.20	651 ± 32	⋯
H21-186962	200.82928	−42.83677	20.00	19.14	0.70	2.84	530 ± 41	⋯

(This table is available in its entirety in machine-readable form.)

metal-poor GCs, metal-rich GCs, and newly confirmed GCs from this study. We fit a Gaussian function to the histogram of the entire GC population, and find a mean velocity of 538 ± 5 km s^{-1} and $\sigma = 134 \pm 4$ km s^{-1}. The mean velocity of the GC system is consistent with the systemic velocity of NGC 5128 of 541 km s^{-1} (Hui et al. 1995) with a velocity dispersion of $\sigma \sim 150$ km s^{-1} (Wilkinson et al. 1986; Silge et al. 2005). Consistent results are found for the metal-rich ($v_{\rm sys} = 535 \pm 9$ km s^{-1}; $\sigma = 139 \pm 7$ km s^{-1}) and metal-poor ($v_{\rm sys} = 538 \pm 7$ km s^{-1}; $\sigma = 131 \pm 5$ km s^{-1}) GC populations when considered separately as well. Many of the GCs associated with the substructures marked in Figure 10 and discussed in Section 5 have relatively low velocities, and excluding these GCs brings the mean velocity to 540 ± 5 km s^{-1}, consistent with the sample as a whole.

We show the radial velocity and velocity dispersion measurements as a function of projected radial distance in Figure 8. W10 found that the metal-poor GCs in NGC 5128 out to 45′ have lower radial velocities in the mean than the metal-rich GCs. In our larger sample we see no difference in the mean velocity between the blue and red GCs, either for the whole sample or restricting it to radii <45′. As seen in the right panel of Figure 8, the velocity dispersion declines slowly from ∼140 km s^{-1} in the central regions to ∼120 km s^{-1} at 25′. At large radii the velocity dispersion goes back up, likely due the presence of unrelaxed substructure (Section 5). The increase of velocity dispersion at large radii is especially prominent in the subsample of metal-poor GCs.

In Figure 9, we again show the radial velocity as a function of the projected radial distance, this time with the symbols denoting the GCs associated with the specific halo substructures from Figure 10. We see that the GCs that are spatially colocated with the individual substructures also tend to cluster in radial velocity, indicating that at least in some cases the GCs and underlying stars are indeed associated coherent structures.

By contrast, other GCs at large radii (80′–110′), even those that clump together at velocities around ∼750 km s^{-1} (Figure 9), are far from each other in projected 2D space and do not appear to be obviously causally connected. It is possible for spatially distant objects to be related in phase space (for example, if they are members of a shell; Merrifield & Kuijken 1998). Small number statistics leading to the false appearance of clustering may also be at play.

5. GCs and Outer Halo Substructures

The outer halo of NGC 5128 is rich with various field substructures in the form of stellar streams and clouds (Crnojević et al. 2013, 2016, 2019). These substructures track the galaxy's active and ongoing merger history. Tidal streams also act as probes of the gravitational potential of the galaxy, and their morphology and kinematics can be used to constrain NGC 5128's dark matter halo mass (Pearson et al. 2022). However, determining the velocities for these low-surface-brightness features is very challenging (Toloba et al. 2016). The kinematics of both tidal structures and dwarfs can sometimes be more easily derived from their associated GCs. Previous work has used GC radial velocities to study both the kinematics of substructure in the halo of M31 (Veljanoski et al. 2014), and to constrain the dynamical mass of dwarf galaxies (e.g., van Dokkum et al. 2016; Toloba et al. 2018).

Crnojević et al. (2016) published a detailed map of the density of RGB stars that shows many substructures and dwarf galaxies in the outer halo of NGC 5128. Figure 10 shows that many of our outer GCs appear spatially associated in projection with prominent stellar features in this map. Furthermore, the GCs associated with these features tend to exhibit similar radial velocities. We note that the RGB map shown here includes PISCeS imaging data available at the time the study of Crnojević et al. (2016) was published, and thus covers a more restricted area than our GC catalog.

In the rest of this section, we consider several of these tentative GC groups and assess the significance of these observed velocity patterns. Identification of the GCs associated with the substructures also is important for our mass analysis in Section 6.

5.1. CenA-Dw1

One of the first discoveries of the PISCeS survey was CenA-Dw1 ($M_V = -13.8$; $r_h = 1.8$ kpc; $R_{\rm CenA,proj} = 93$ kpc) and its possible companion CenA-Dw2 ($M_V = -9.7$; $r_h = 0.4$ kpc; $R_{\rm CenA,proj} = 92$ kpc), which are only separated by ∼3 kpc on the sky (Crnojević et al. 2014, 2019). Inspection of follow-up Hubble Space Telescope imaging of the CenA-Dw1 field revealed four clear, semiresolved GCs associated with CenA-Dw1. All of these were GC candidates in the H21 sample, and were targeted for spectroscopic follow up using the high-
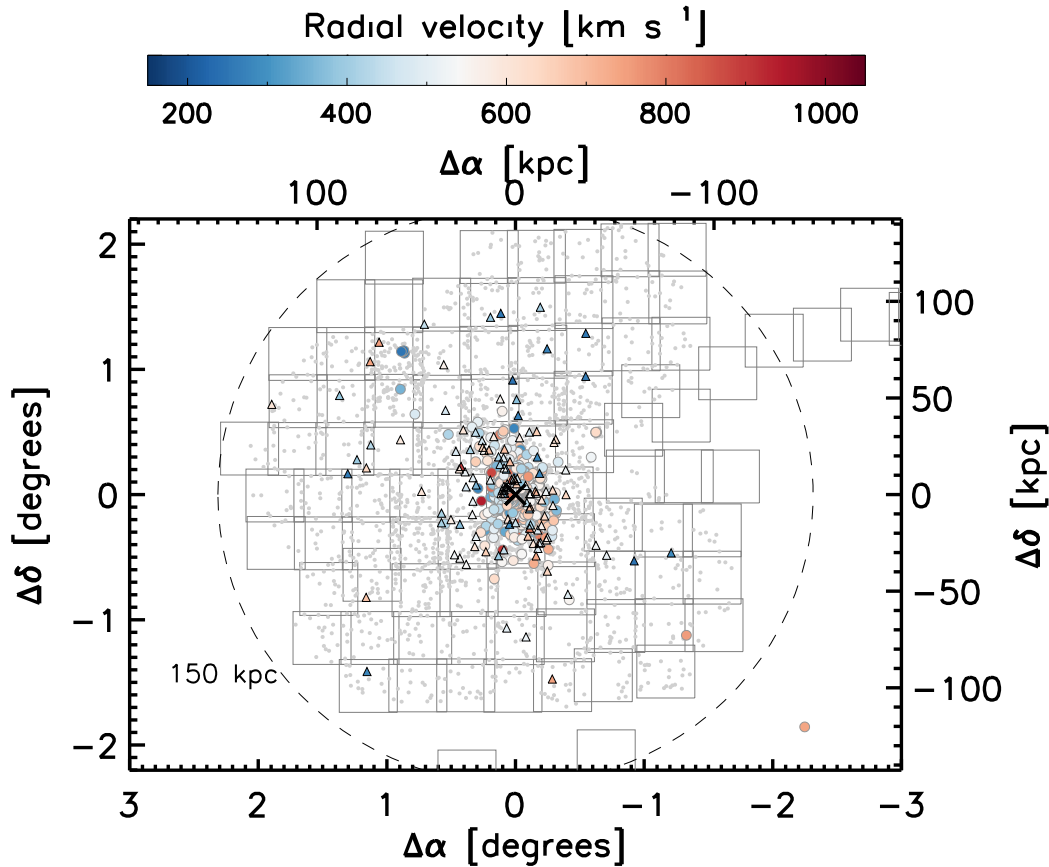
Figure 4. Positions of all confirmed GCs in NGC 5128 with radial velocity measurements, where the symbol colors correspond to radial velocity. The triangles mark newly identified GCs, and the circles mark previously confirmed GCs. To demonstrate our observing coverage, the gray points mark the positions of spectroscopically observed targets that were not confirmed to be GCs and the squares denote the footprint of the PISCeS survey. An "x" marks the center of NGC 5128, with a velocity of 541 km s^{-1}.

resolution mode of M2FS as presented in Dumont et al. (2022). These were all confirmed to be GCs, and indeed they have velocities within ≈ 14 km s^{-1} of each other, as would be expected for the GC system of a faint dwarf galaxy; see Figure 9.

The four CenA-Dw1 GCs are between $\approx 5''$ and $60''$ (≈ 90–1140 pc) from the center of the dwarf in projection, and have absolute magnitudes ranging between $M_V = -7.0$ and -8.7 mag. The brightest GC ($r_0 = 19.0$; $M_V = -8.7$ mag) is located closest to the dwarf center and could potentially be a nuclear star cluster, as these are often slightly offset from the galaxy center (e.g., Georgiev et al. 2009). Taking the weighted mean velocity of all four GCs, we find $v = 265 \pm 3$ km s^{-1} (262 ± 3 km s^{-1} if the central cluster is removed). Within the precision of our measurements, the intrinsic velocity dispersion of this GC system is consistent with zero. If CenA-Dw1 had a mass-to-light ratio similar to the Fornax dwarf galaxy (Walker et al. 2007), the velocity dispersion would be $\gtrsim 10$ km s^{-1}, which should have been detectable given our GC velocity uncertainties in most instances. This preliminary result is intriguing and should motivate future, more precise radial velocity measurements (of both the dwarf and its GCs) that would allow the determination of the dynamical mass of CenA-Dw1.

5.2. CenA-MM-Dw3 and Its Tidal Tails

One of the most striking substructure features is CenA-MM-Dw3, a disrupting dwarf galaxy positioned to the northeast of the galaxy center with tidal tails spanning over 1°.5 (Crnojević et al. 2016). A confirmed GC (H21-360500) sits at the center of the main remnant of the disrupting dwarf. This object has a velocity of 359 ± 2 km s^{-1} and is likely the dwarf's nuclear star cluster (Dumont et al. 2022), so we take this velocity as the best estimate of that for the dwarf. Note that the observed blueshifted line-of-sight velocity of Dw3 with respect to NGC 5128 is consistent with the corotating line-of-sight velocity trend found by Müller et al. (2021) for 21 out of 28 of NGC 5128's satellites with measured velocities. However, the proper motion predictions from Pearson et al. (2022) moves Dw3 in a direction out of the planar satellite structure of NGC 5128 (Müller et al. 2018).

Projected along the tidal tails are an additional five NGC 5128-confirmed GCs with measured radial velocities, which have velocities within ~ 100 km s^{-1} of the dwarf's systemic velocity. The spatial locations of the GCs in the outer regions of the stream, and possible offsets from the main body of the stream, would be consistent with a GC population that started as more extended than the stars in the dwarf, and which would have begun to be tidally stripped earlier than the bulk of the stars in the dwarf.

Figure 11 plots the velocities of these GCs as a function of distance from the center of CenA-MM-Dw3. Also plotted is a range of stream models from Pearson et al. (2022), who explored dynamical models that could reproduce the stream morphology and velocity of the central star cluster associated

Table 5
Foreground Stars and Background Galaxies in the Vicinity of NGC 5128

H21-ID	R.A. (deg J2000)	Decl. (deg J2000)	g (mag)	r (mag)	Weighted v_r (km s^{-1})	Type
H21-045317	199.13075	−43.57504	19.97	19.04	4 ± 14	star
H21-048213	199.19358	−43.48774	21.45	19.76	−418 ± 12	star
H21-048293	199.19549	−43.57120	19.32	18.46	91 ± 17	star
H21-049729	199.22672	−43.35489	21.18	20.52	−377 ± 20	star
H21-054879	199.33153	−43.54923	19.90	19.29	280 ± 15	star
H21-055213	199.33754	−43.33671	19.58	18.24	−4 ± 22	star
H21-055349	199.33936	−43.97305	21.18	20.12	−18 ± 16	star
H21-059335	199.39602	−43.17051	20.21	19.29	−37 ± 20	star

(This table is available in its entirety in machine-readable form.)
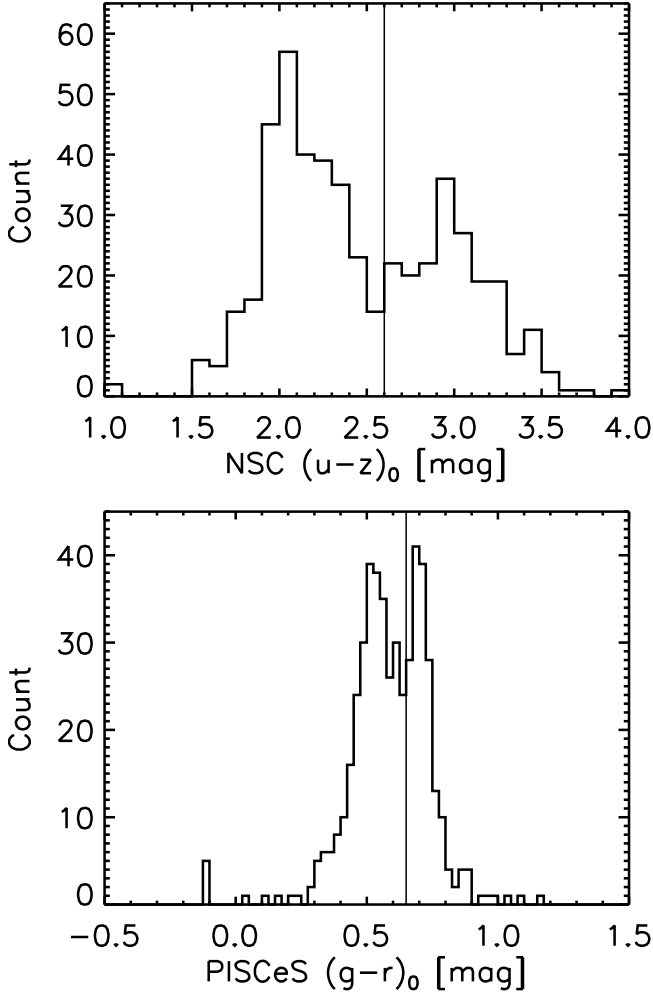
Figure 5. The confirmed GCs in NGC 5128 show a bimodal color distribution, which we use to split them into metal-poor (blue) and metal-rich (red) subpopulations. The top histogram shows the $(u - z)_0$ color from the NSC and bottom histogram shows the $(g - r)_0$ color from PISCeS for the same set of GCs, where the photometry for both have been corrected for foreground extinction. The vertical lines show the adopted divide between the two subpopulations, at $(u - z)_0 = 2.6$ and $(g - r)_0 = 0.65$ mag.

Figure 6. Binned surface density profiles for the velocity-confirmed GCs with $20.5 > r > 17.5$, showing the steeper radial profile of the metal-rich GCs than the metal-poor GCs. The samples are all GCs (black circles, median 25 GCs per annulus), metal-poor GCs (blue squares, median 14 per annulus), and metal-rich GCs (red triangles, median 12 per annulus). The overplotted power-law fits are made from radii 7′–30′; these fitting limits are denoted with dotted lines. Within 7′, the surface density profiles flatten due to incompleteness.

with CenA-MM-Dw3. While the models leave some freedom in the best-fit orbital parameters of the stream, they are representative of the family of models that best match the existing data. The models both reproduce the stream morphology and the velocity of the central Dw3 star cluster even though they were not fit against the new GC velocities presented here. Note, however, that the sign of the velocity gradient would flip if Dw3 was instead located in front of NGC 5128; the plotted set of models assume that Dw3 is at a slightly larger distance from us than NGC 5128. Also, three of the GCs we associated with CenA-MM-Dw3 and its tidal tail are beyond what Pearson et al. (2022) considered the extent of the stream.

This comparison suggests that at most three GCs are associated with CenA-MM-Dw3: the central nuclear star cluster and two GCs in the tidal tails. In this case the GCs would generally follow the predicted velocity gradient, and the other objects would be unassociated with the dwarf. It is likely not tenable for all the GCs to have originated from the dwarf; while Pearson et al. (2022) does not make a specific prediction for the velocity dispersion at specific distances along the stream, the dispersion should reflect that of the progenitor and
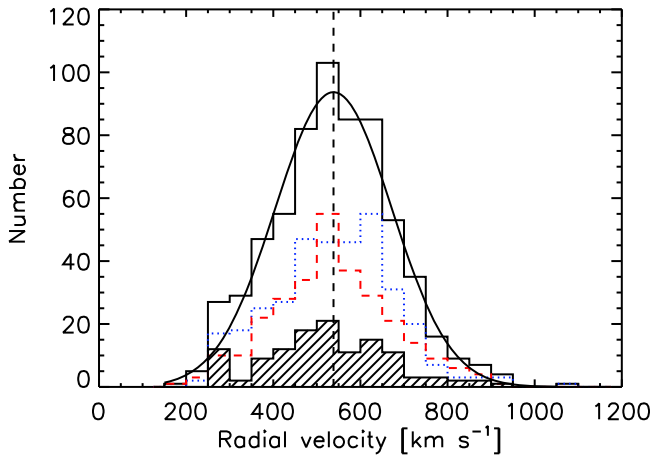
Figure 7. Radial velocity distributions of the full confirmed GC population (tall histogram), newly confirmed GCs (hatched histogram), and metal-poor (blue dotted) and metal-rich (red dashed) subpopulations. We also overplot a Gaussian fit to the entire data set (see Section 4.2).

is expected to be low. For example, the intrinsic velocity dispersion along the tidal tails of the Sgr dwarf is only ∼15 km s^{-1} (e.g., Vasiliev & Belokurov 2020), and the luminosity and other characteristics of CenA-MM-Dw3 are consistent with it having had an Sgr-like progenitor. Hence deviations of at most ∼30–35 km s^{-1} from the mean stream velocity at a given radius would be expected, compared to the observed deviations of >100 km s^{-1} that would be needed to accommodate all of the candidate stream GCs as truly associated with CenA-MM-Dw3. It is also plausible that even fewer than three GCs are linked to the dwarf.

Given its importance for constraining the properties of the dark matter halo of NGC 5128, such as its shape and mass profile, searching for additional GCs that could be associated with CenA-MM-Dw3 (i.e., fainter systems) should be a high priority moving forward. The six currently known GCs that lie projected atop DW3 have $20.9 > r > 21.9$ mag. The area around CenA-MM-Dw3 was primarily observed with AAT/ AAOmega, which detected GCs in NGC 5128 down to a magnitude of $r \approx 21.5$ mag. There are many GC candidates that lie on top of the stream that did not have observations with high enough S/Ns to determine their classification, but we will pursue these in future work.

5.3. Second Stream

The "second stream" is a stellar feature seen in resolved RGB stars that is directly south of CenA-MM-Dw3, but much less luminous (Crnojević et al. 2016). It appears to lack a remnant central concentration of stars, suggesting the progenitor dwarf has been fully disrupted. Here we identify two GCs with similar velocities that lie projected on top of the second stream, and have velocities within 60 km s^{-1} of each other. Initial simulations were able to reproduce the general stream morphology using the central GC velocity as an initial condition (Pearson et al. 2022), and future refinements may provide tighter constraint on the properties of NGC 5128's dark matter halo in conjunction with the Dw3 stream.

5.4. Cloud S

Another stellar substructure identified by Crnojević et al. (2016) is "Cloud S," a large, diffuse structure south of the main body of NGC 5128. The boundaries of Cloud S are somewhat

difficult to define. It is not clear whether there is a single structure from one accretion event or multiple overlapping substructures. There are at least six GCs that lie in projection on this structure (Figure 10). These GCs have a mean velocity of 524 km s^{-1} and a dispersion of only 19 km s^{-1} (the low dispersion is apparent in Figure 9), suggesting a low-mass progenitor. If the single highest velocity is removed as a possible interloper, the velocity dispersion drops to only 13 km s^{-1}, consistent with an unresolved intrinsic dispersion given the typical velocity uncertainties for these GCs. In either case, the low dispersion suggests that the association between the GCs and Cloud S could be real. An extension of the stellar RGB map to the west of Cloud S could allow better mapping of these substructures and an improved judgment about the association of GCs with Cloud S.

6. Kinematics and Dynamics of NGC 5128

There is a broad range of efforts in the existing literature to provide mass estimators for pressure-supported systems (e.g., Bahcall & Tremaine 1981; Richstone & Tremaine 1986; Strigari et al. 2008; Wolf et al. 2010). The goal of these estimators—all of which are essentially variations on the virial theorem—is to allow basic mass measurements that do not require complex dynamical modeling. These estimators all use simplifying assumptions about the spatial distribution and orbital properties of the tracer population, leading to various systemic uncertainties in the resulting masses.

Here we make a hybrid mass estimate of NGC 5128, combining two different estimators that account for both the pressure-supported (M_p) and rotationally supported (M_r) mass components of NGC 5128, summing these to get the total mass. A similar kinematic analysis of NGC 5128 was performed by W10 with the GC population available at the time. We emphasize that this is a preliminary dynamical analysis that will be supplanted by a more sophisticated model in a future paper.

For the pressure-supported component, we use the "tracer mass estimator" (Evans et al. 2003), which is well suited for tracer populations such as GCs that do not necessarily follow the underlying radial distribution of the dark matter.

This mass M_p is given by:

$$M_p = \frac{C}{GN} \sum_i (v_{f_i} - v_{\mathrm{sys}})^2 R_i, \qquad (1)$$

where N is the number of objects in the sample, v_{f_i} is the measured radial velocity of the tracer object with any rotational amplitude removed, v_{sys} is the systemic velocity, and R_i is the projected galactocentric radius of the tracer object. We determine the systemic velocity, rotation amplitude, and projected rotation axis for the GC system using the kinematic solution described in Section 6.1.

The constant C is dependent on the shape of the underlying gravitational potential, the radial distribution of the tracers, and the anisotropy of the system. For this estimate, we assume the GC system is spherical and isotropic, so the value of the constant C is given by:

$$C = \frac{4(\alpha + \gamma)(4 - \alpha - \gamma)(1 - \left(\frac{r_{\mathrm{in}}}{r_{\mathrm{out}}}\right)^{(3-\gamma)})}{\pi(3 - \gamma)(1 - \left(\frac{r_{\mathrm{in}}}{r_{\mathrm{out}}}\right)^{(4-\alpha-\gamma)})}, \qquad (2)$$
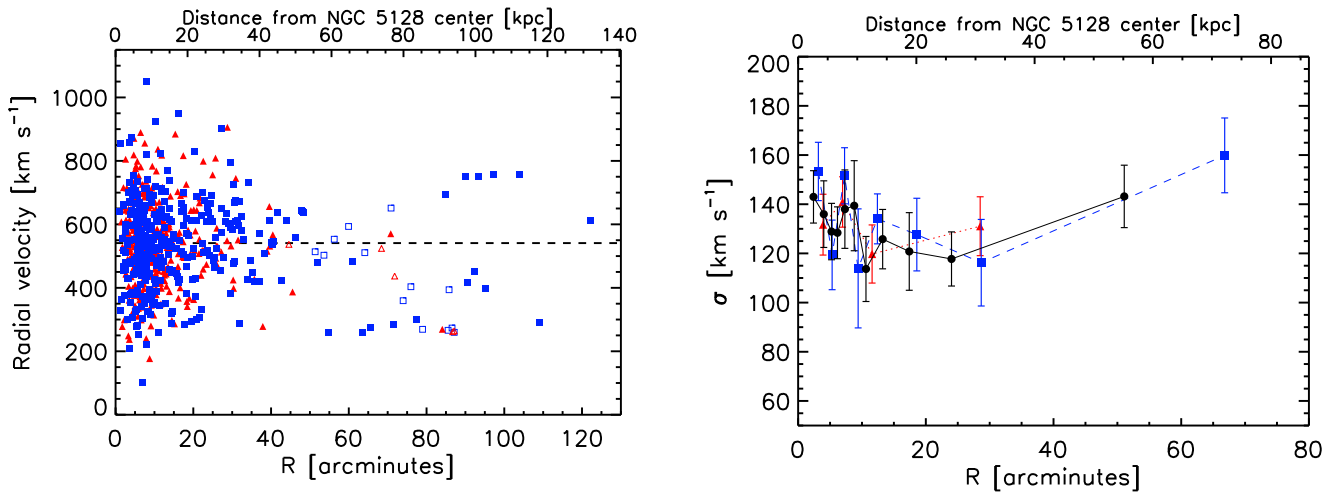
Figure 8. Left: radial velocity measurements for the confirmed metal-rich (red triangles) and metal-poor (blue squares) GCs as a function of projected galocentric radius, where the open symbols denote GCs in the substructures marked in Figure 10 and the filled symbols are all other GCs. The horizontal dashed line marks the systemic velocity of 541 km s^{-1} for NGC 5128. Right: the velocity dispersion as a function of radius for all GCs (black circles), binned by groups of 57 GCs, using a maximum likelihood estimator (e.g., Pryor & Meylan 1993). Also shown are measurements for the metal-rich (red triangles) and metal-poor (blue squares) GCs, binned by groups of 71 and 44 GCs, respectively.

where r_{in} and r_{out} are the 3D radii corresponding to the 2D projected radii R_{in} and R_{out} of the innermost and outermost tracers in the sample, respectively. Because our GC tracers are derived from a wide-angle survey in which the population is traced out to large radii, we assume that $r_{out} \approx R_{out}$ and $r_{in} \approx R_{in}$. We assume an isothermal halo over the radial range of our data, which corresponds to $\alpha = 0$. The parameter γ is calculated from the surface density of the tracer population derived in Section 4.1, with values of 3.69 ± 0.19, 3.64 ± 0.27, and 4.05 ± 0.28 for the total, blue, and red subpopulations, respectively.

The mass supported by rotation is determined from the rotational component of the Jeans equation:

$$M_r = \frac{R_{out}(\Omega R)^2}{G},$$ (3)

where R_{out} is again the projected radius of the outermost tracer in the sample and ΩR is the rotation amplitude (amount of rotation). We assume here that the rotation of the halo GCs occurs only on simple circular orbits.

The values of the rotation parameters and mass estimates are shown in Table 6 and discussed in the following sections.

6.1. Rotation Parameters

To determine the rotation parameters for the updated GC population, we use the equation:

$$v_p = v_{sys} + \Omega R \sin(\Theta - \Theta_0),$$ (4)

described in Côté et al. (2001), where v_p is the measured radial velocity, v_{sys} is the systemic velocity, ΩR is the rotation amplitude, Θ is the measured angular position on the projected sky in degrees east of north, and Θ_0 is the rotation axis in the plane of the sky, also in degrees east of north. The assumptions made include: (i) the GC system of NGC 5128 can be approximated as spherical; (ii) its angular velocity field is constant in spheres; and (iii) its rotation axis lies exactly on the plane of the sky. The individual GCs are weighted according to

their individual radial velocity uncertainties, where the radial velocities and associated uncertainties used are the weighted averages of all previous measurements, as listed in Tables 3 and 4.

Our fitting results for the entire GC sample as well as the metal-rich and metal-poor subpopulations are shown in Figure 12. The best-fit sine curves clearly show the large dispersion of the GC system with a small rotational component. The rotation parameters are listed for subsets of the GC population in Table 6, where errors are calculated using a Monte Carlo bootstrapping method (resampling with replacement).

By comparing the rotation parameters for the sample of all GCs to the sample of GCs unassociated with substructures in the halo, we checked that the substructure-associated GCs do not greatly affect the rotation parameters of the system as a whole.

Stronger differences can be seen when comparing the rotation parameters of the metal-poor and metal-rich GCs. The metal-rich GC subpopulation has a larger rotation amplitude than the metal-poor GC subpopulation. Both metallicity subpopulations appear to rotate around the isophotal major axis of the galaxy within $\sim15'$. Similar kinematic trends were seen in the kinematic analysis by W10, based on a smaller sample of NGC 5128 GCs that extended out to 45$'$ in galactocentric radius. Comparing to other galaxies, some evidence for rotation around the photometric major axis has previously been observed for GCs over some radial ranges in the giant ellipticals NGC 4472 (Zepf et al. 2000; Côté et al. 2003) and M87 (Côté et al. 2001; Strader et al. 2011).

6.2. Mass Results

We determine the rotation- and pressure-supported masses in cumulative bins of increasing radii. The results are tabulated in Table 6 with columns displaying the GC subpopulation, the outer radial range of the included GCs in arcminutes, the number of GCs per radial bin, the systemic velocity, the rotation amplitude, the rotation axis, the pressure-supported mass, the rotation-supported mass, the total mass enclosed, and
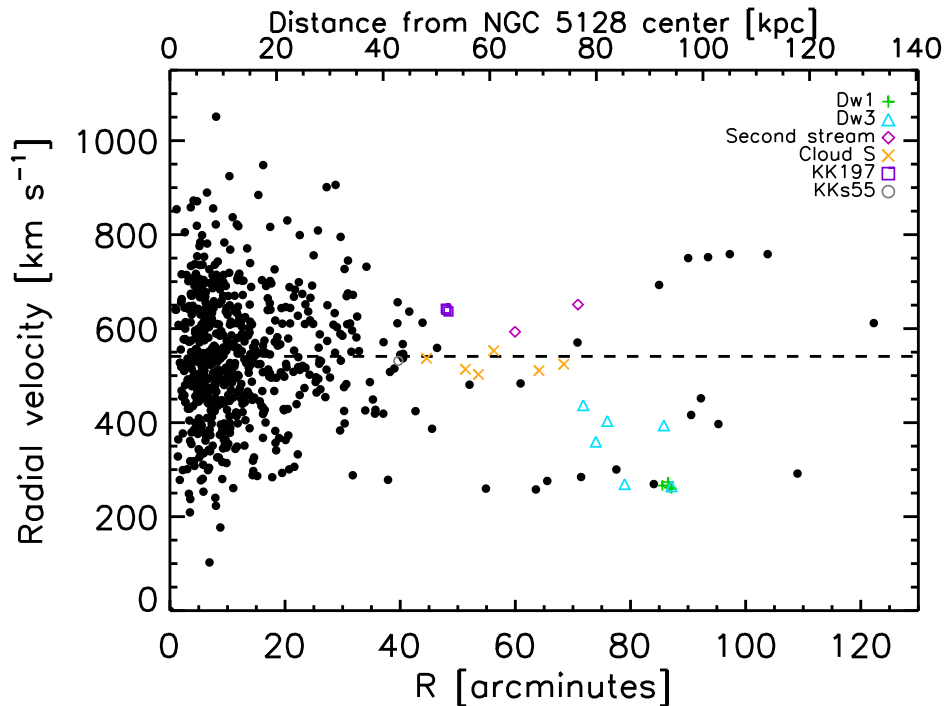
Figure 9. Radial velocity measurements for the confirmed GCs as a function of the projected galactocentric radius, where the colored symbols denote GCs associated with the substructures marked in Figure 10 and the black dots are all other GCs. The horizontal dashed line marks the systemic velocity of 541 km s^{-1} for NGC 5128.

finally the outer radial range of the included GCs in kiloparsecs. Mass errors are calculated using a Monte Carlo bootstrapping method. We use an inner radial limit of 5′ for all tabulated results. As a small number of GCs do not have photometry available, they cannot be classified by subpopulation, causing the number of metal-poor and metal-rich GCs in a given radius range to be less than the number listed in the corresponding row of the "All" range.

An important issue is that the tracer mass estimator technique assumes a well-behaved, virialized population, but some of the outer halo GCs appear to be spatially associated with cold stellar debris, leading to both biased and correlated velocities. Therefore, we list values for the total mass with ("All") and without ("Field") the GCs that are potentially associated with substructure in the halo of NGC 5128 noted in Figure 10 (CenA-Dw1, CenA-MM-Dw3, Second Stream, Cloud S, KK197, and KKs55). Despite these efforts to exclude GCs associated with accretion events, it is possible that GCs at large radii are not in equilibrium (see also, e.g., Coccato et al. 2013), and that such measurements from a handful of tracers should be treated with caution.

We made two additional assumptions that may lead to additional uncertainties in our masses: that the GC orbits are isotropic, and that the whole dark matter halo is isothermal. These potential sources of systematic uncertainty are not incorporated into the formal mass uncertainties. Evans et al. (2003) report a typical systematic uncertainty due to anisotropy of about 30%. For substantial deviations from an isothermal halo profile, the masses could differ by 40%–50%, though such large variations around the halo scale radius might be surprising. Uncertainties of this order are plausible, especially in the outer regions of NGC 5128's halo.

Table 6 shows that at all radii and for all samples, rotational support is not important compared to pressure support, contributing at most a few percent to our GC-based mass

estimates. It also shows that the metal-rich and metal-poor subpopulations generally give consistent mass estimates within their respective uncertainties. The errors for the mass measurements were calculated using the bootstrap method of standard error.

We briefly highlight the masses inferred from our analysis at a few specific radii. First, we find an $R < 20'$ (21.6 kpc) mass of $5.1 \pm 0.6 \times 10^{11}$ $M_\odot$. This radius is likely not too far from the dark matter halo scale radius (which is not directly constrained in this modeling). Next, within $R < 60'$ (~65 kpc) the enclosed mass is 1.2×10^{12} $M_\odot$ for both the "All" sample and "Field" sample of GCs. This is the largest radius at which the GC population appears dominated by a relaxed, mostly virialized population, though some GCs associated with substructures are present even at these radii.

Finally, using the "Field" GCs unassociated with kinematically cold substructure, we find the total mass enclosed within $110'$ ($\approx$120 kpc) from the center of NGC 5128 to be $(2.5 \pm 0.3) \times 10^{12}$ $M_\odot$. This is around where the sampling peters out: if one calculates the mass extending to the most remote known NGC 5128 cluster at $175'$ ($\approx$190 kpc), the value is $(3.2 \pm 0.6) \times 10^{12}$ $M_\odot$, likely nearing the virial radius of the galaxy. But there are only two objects in the sample between $110'$ and $175'$, and tracers at the largest radii are likely not in equilibrium, so this "virial" measurement is primarily an extrapolation of the ~120 kpc value.

6.3. Comparison to Previous Measurements

There are a number of mass estimates found in the literature that sample a similar spatial range as to our work here, which are listed in Table 7 and plotted in Figure 13.

Peng et al. (2004b) used 215 GCs extending out to 40 kpc (~36′) to estimate a pressure-supported mass of 7.5×10^{11} $M_\odot$ (see Woodley et al. 2007 for this mass, corrected from Peng
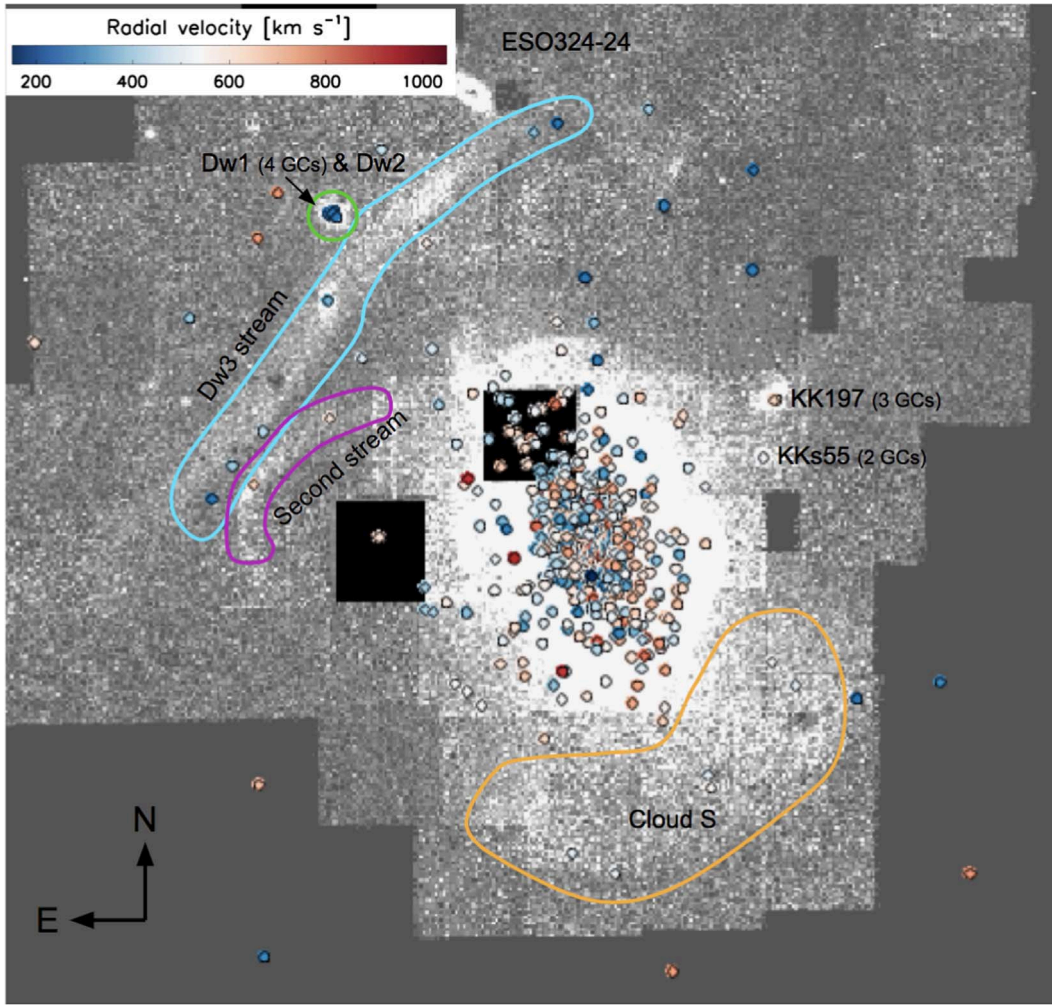
Figure 10. RGB map of NGC 5128 from PISCeS. The positions of known GCs are marked with colored dots that correspond to their weighted radial velocity measurements. The colored contours mark the cold stellar features of interest discussed in the text. We refer the reader to Figures 4 and 9 for further context.
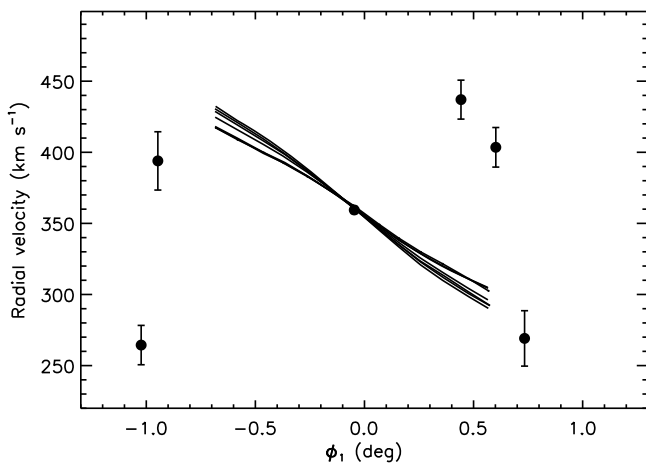

Figure 11. Radial velocity as a function of distance from the position of the main galaxy remnant for the six GCs that lie projected on top of the CenA-MM-Dw3 stream. Overplotted are a series of dynamical models for the predicted radial velocity gradient along the stream presented in Pearson et al. (2022). The x-axis coordinate (ϕ_1) is adopted from Pearson et al. (2022), and represents the longitude in a coordinate system centered on NGC 5128 and rotated such that Dw3 is at $\phi_1 = 0°$. As we discuss in Section 5.2, it is not likely that all of the GCs projected onto the Dw3 stream are physically associated with it.

et al. 2004b). We reevaluate the pressure-supported mass using the newly updated sample of GCs out to 36′ and obtain $M_p = 8.4 \pm 0.8 \times 10^{11} M_\odot$. Woodley et al. (2007) and W10 measured $M_t = (13 \pm 5) \times 10^{11} M_\odot$ within 50 kpc and $M_t = (10.7 \pm 3.5) \times 10^{11} M_\odot$ within 45′ (49 kpc). While not directly tabulated in Table 6, we evaluate our total mass estimate within 50 kpc and find $M_t = (10.5 \pm 1.0) \times 10^{11} M_\odot$. These mass estimates match well within the measurement uncertainties.

Based on X-ray emission from the interstellar medium and the inner radio lobes, Kraft et al. (2003) find that within 15 kpc (13.′8) of the nucleus, the total mass of NGC 5128 is $\sim 2 \times 10^{11} M_\odot$. Within this same projected radius, we find $M_t = (3.6 \pm 0.4) \times 10^{11} M_\odot$.

Peng et al. (2004c) measured the total mass of NGC 5128 using planetary nebulae to be $10.6 \times 10^{11} M_\odot$ within 80 kpc (see Woodley et al. 2007 for this mass, corrected from Peng et al. 2004b). Woodley et al. (2007) similarly found $M_t = (10 \pm 2) \times 10^{11} M_\odot$ within 90 kpc. All the GCs in our sample at radii between 80 and 90 kpc (74′–83′) are located within kinematically cold substructures. So our closest comparable measurement is $M_t = (16.6 \pm 2.2) \times 10^{11} M_\odot$ within 80′, based on the "farthest" field GC at 71′ (76 kpc).

Table 6
The Mass of NGC 5128

GCs	outer R (arcminutes)	N	$v_{\rm sys}$ (km s^{-1})	ΩR (km s^{-1})	Θ_0 (deg. E of N)	M_p ($\times 10^{11}$ $M_\odot$)	M_r ($\times 10^{11}$ $M_\odot$)	M_t ($\times 10^{11}$ $M_\odot$)	Outer R (kpc)
All GCs	10	221	535 ± 13	48 ± 37	192 ± 172	2.71 ± 0.45	0.063 ± 0.049	2.78 ± 0.49	10.8
All GCs	20	387	532 ± 9	54 ± 16	175 ± 32	4.97 ± 0.52	0.146 ± 0.070	5.10 ± 0.57	21.6
All GCs	30	454	538 ± 8	43 ± 17	175 ± 39	6.99 ± 0.62	0.137 ± 0.076	7.14 ± 0.66	32.4
All GCs	40	485	539 ± 7	48 ± 13	170 ± 23	9.08 ± 0.82	0.231 ± 0.113	9.30 ± 0.89	43.2
All GCs	60	504	540 ± 7	45 ± 13	169 ± 20	11.82 ± 1.21	0.303 ± 0.155	12.13 ± 1.31	64.8
All GCs	80	517	537 ± 7	46 ± 15	170 ± 25	17.77 ± 2.36	0.422 ± 0.211	18.19 ± 2.49	86.4
All GCs	100	531	534 ± 7	48 ± 15	165 ± 23	27.59 ± 3.67	0.553 ± 0.295	28.14 ± 3.84	108.0
All GCs	110	533	535 ± 8	50 ± 14	165 ± 23	30.71 ± 4.28	0.674 ± 0.301	31.43 ± 4.44	118.8
All GCs	175	535	536 ± 7	50 ± 14	164 ± 21	38.55 ± 6.97	0.908 ± 0.492	39.56 ± 7.28	189.0
Field GCs	60	499	540 ± 7	47 ± 12	168 ± 17	11.35 ± 1.22	0.305 ± 0.142	11.62 ± 1.30	64.8
Field GCs	80	505	539 ± 7	47 ± 13	167 ± 23	16.15 ± 2.09	0.416 ± 0.206	16.58 ± 2.21	86.4
Field GCs	100	513	539 ± 8	46 ± 14	165 ± 23	21.14 ± 2.53	0.505 ± 0.259	21.63 ± 2.66	108.0
Field GCs	110	515	539 ± 7	48 ± 14	166 ± 31	24.25 ± 3.14	0.608 ± 0.294	24.84 ± 3.28	118.8
Field GCs	175	517	541 ± 7	47 ± 12	164 ± 16	30.56 ± 5.29	0.826 ± 0.454	31.50 ± 5.55	189.0
MP GCs	20	202	539 ± 13	43 ± 25	169 ± 69	4.86 ± 0.77	0.094 ± 0.095	4.96 ± 0.83	21.6
MP GCs	40	264	549 ± 11	35 ± 20	168 ± 62	8.67 ± 1.15	0.116 ± 0.127	8.78 ± 1.23	43.2
MP GCs	60	280	549 ± 10	34 ± 20	165 ± 71	11.63 ± 1.74	0.166 ± 0.180	11.79 ± 1.86	64.8
MP GCs	80	290	545 ± 10	34 ± 20	163 ± 68	19.85 ± 3.62	0.227 ± 0.249	20.18 ± 3.76	86.4
MR GCs	20	182	533 ± 13	63 ± 23	178 ± 120	6.10 ± 0.97	0.197 ± 0.102	6.30 ± 1.05	21.6
MR GCs	40	218	533 ± 11	62 ± 19	172 ± 64	11.72 ± 1.78	0.379 ± 0.186	12.12 ± 1.91	43.2
MR GCs	60	221	532 ± 11	61 ± 21	172 ± 52	12.85 ± 2.11	0.410 ± 0.218	13.26 ± 2.27	64.8
MR GCs	80	224	532 ± 11	62 ± 18	173 ± 63	18.23 ± 3.16	0.677 ± 0.331	18.93 ± 3.40	86.4

Note. Field GCs are taken from the "All GCs" sample but with those GCs associated with clear stellar substructures removed. MP GCs are from the metal-poor GC sample defined in Section 4.1. MR GCs are from the metal-rich GC sample defined in Section 4.1.
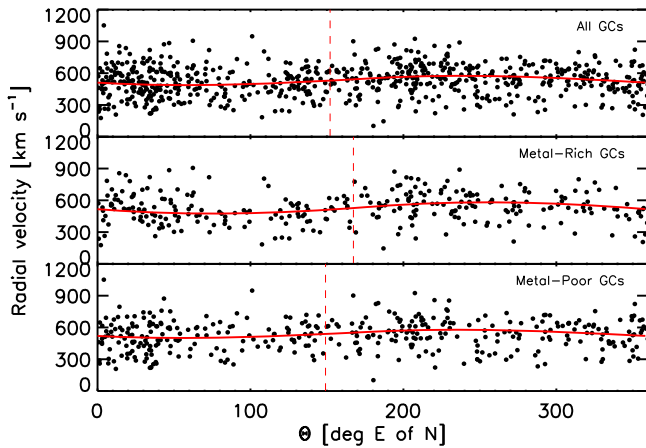
Figure 12. Position angles and measured radial velocities are shown for the entire GC sample (top), the metal-rich sample (middle), and the metal-poor sample (bottom). Each GC sample has been fit with Equation (4), which is overplotted as the red solid curve. The dashed vertical line denotes the fitted rotation axis of each sample. The fitted parameters are listed in Table 6.

Most recently, Pearson et al. (2022) used the morphology of Dw3 and its stellar stream in conjunction with the velocity of the central Dw3 star cluster to constrain the mass of NGC 5128 assuming an Navarro–Frenk–White (NFW) dark matter halo profile. Given this, we list the range of masses allowed at a fiducial radius of 40 kpc in these models in Table 7, $M_t = (9.9 \pm 2.7) \times 10^{11}$ $M_\odot$, which is in excellent agreement with our GC measurements.

We also list two mass measurements of NGC 5128 at larger radii based on dwarf galaxy kinematic modeling in Table 7 (Karachentsev et al. 2007; Müller et al. 2022); while these measurements are beyond the radii in the current work, they are consistent with extrapolations of our data to large radii.

Overall, we find reasonable to excellent agreement with the previous masses based on GCs, but tend to find higher masses than the previous estimates based on planetary nebulae, likely due to differing anisotropies between these populations not captured in the assumptions of this initial simple modeling.

7. Summary

We present new radial velocity measurements for 175 previously known and 121 newly confirmed GCs in NGC 5128. Our spectroscopy was taken between 2017 and 2022 with Magellan/M2FS and AAT/AAOmega. We discovered 69 new GCs within 30′ and 28 new GCs beyond 50′, showcasing the continued need for spectroscopy of GC candidates at all radii. We found that 27% of priority sample GC candidates were confirmed to be true GCs, compared to only 7% of those that were not in the priority sample; the fraction of true GCs in the priority sample soars to 68% within 30′ of NGC 5128. The population of confirmed GCs now extends out to a projected radius of nearly 190 kpc. This enables us to explore the kinematic properties of the GCs located in the outermost halo of NGC 5128 for the first time.

We test the fidelity of our velocity measurements by comparing to the catalogs of W10 and find excellent agreement, with the measurements for nearly all individual

Table 7
Mass Estimates for NGC 5128 from Recent Literature

Reference	M_t (10^{11} $M_\odot$)	R_{max} (kpc)	Method
Kraft et al. (2003)	~2	15	X-ray emission
Pearson et al. (2022)	9.9 ± 2.7	40	Stream modeling
W10	10.7 ± 3.5	49	Dynamical tracers: GCs
Woodley et al. (2007)	13 ± 5	50	Dynamical tracers: GCs
Peng et al. (2004c)	10.6	80	Dynamical tracers: PNe[1]
Woodley et al. (2007)	10 ± 2	90	Dynamical tracers: PNe
This work	32 ± 6	190	Dynamical tracers: GCs
Karachentsev et al. (2007)	64–81	400	Orbital/virial; Dynamical tracers: dwarf galaxies

Note. 1. See Woodley et al. (2007) for this mass, corrected from Peng et al. (2004c).
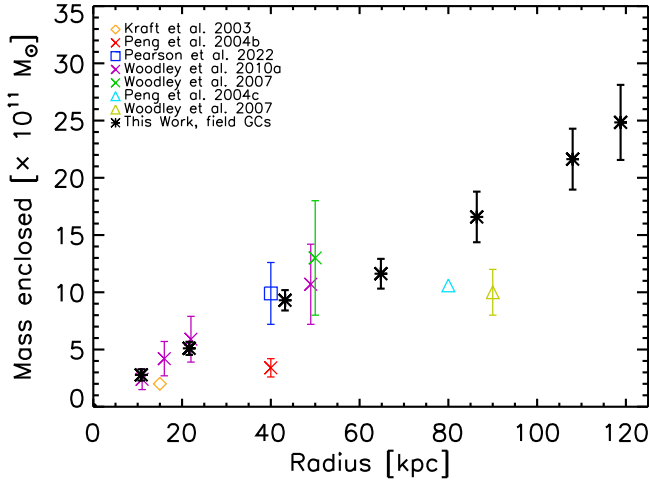
Figure 13. Enclosed mass estimates for NGC 5128 using different techniques, expressed in 10^{11} $M_\odot$. The method for each technique is listed in Table 7.

GCs within the measurement uncertainties. We remeasured velocities for four GCs with conflicting measurements that were listed in H21, and find that with the new radial velocity measurements, they can be more confidently classified as GCs (see Section A.2).

Using the measurements presented here, we demonstrate that various discrete groups of GCs projected onto the most luminous halo streams and overdensities exhibit clear kinematic patterns. This indicates that a substantial fraction of the outer halo GC population consists of objects accreted along with their now-defunct host galaxies, as has been shown for M31 (Mackey et al. 2010; Veljanoski et al. 2014). A striking feature of many of the ensembles we considered is the coldness of their kinematics, most clearly shown by the low velocity dispersions of GCs associated with CenA-Dw1 and Cloud S, but potentially also with the CenA-MM-Dw3 stream. Definitive proof of these associations will require additional follow-up observations and more modeling.

Based on color, we divide the confirmed GCs into metal-poor $((g - r)_0 < 0.65)$ and metal-rich subpopulations. We find that the radial distribution of the metal-rich subpopulation has a steeper slope and is more centrally concentrated, which follows trends seen in other extragalactic studies (e.g., Brodie & Strader 2006; Faifer et al. 2011; Forbes et al. 2012). The metal-poor population is more radially extended, and there are more metal-poor GCs than metal-rich GCs beyond ~9′. Additionally, ≈80% of the GCs associated with halo substructures are metal poor, providing evidence for the ongoing buildup of its halo via the accretion of lower-mass galaxies.

We find an overall rotation signature of the GC population at all radii. This rotation is not driven by GCs clearly associated with underlying substructures. Comparing the rotation of the metal-poor and metal-rich GC subpopulations, we find while they have similar projected rotation axes, the metal-rich GCs have a larger rotation amplitude than the metal-poor GCs at all radii. This is in contrast with observations in the Milky Way where the halo GC population appears to exhibit at most only a mild net rotation (e.g., Harris 2001; Brodie & Strader 2006), though in M31 the metal-poor GCs have significant rotation, albeit at half the rate of the most metal-rich clusters (Caldwell & Romanowsky 2016).

We use the GC velocities to estimate the enclosed mass of NGC 5128 at a range of radii using a tracer mass estimator. We find a dynamical mass of $1.2 \pm 0.1 \times 10^{12}$ $M_\odot$ ($2.5 \pm 0.3 \times 10^{12}$ $M_\odot$) within a radius of ~65 kpc (~120 kpc), but this result is preliminary, and we will present detailed dynamical modeling in a follow-up work (A. Dumont et al. 2023, in preparation).

Appendix A
Discussion of Conflicting Velocity Measurements

In this Appendix, we discuss several types of "conflicting" NGC 5128 GC velocity measurements. The first corresponds to new NGC 5128 GC measurements which disagree with the weighted radial velocity measurements reported in W10 by $>2\sigma$, and can be seen as outliers in Figure 3. The second corresponds to velocity measurements in the literature of the same GC which are in conflict with each other, and which we were able to resolve by obtaining a new velocity measurement. In the final case, the reported velocities (either in the literature or here) could be consistent with a GC, but Gaia DR3 provides evidence that the source is a foreground star.

In all cases of GCs with discrepant measurements, we visually checked the PISCeS data for close companions to rule out target misidentification, but found no viable interlopers.

A.1. Outlier New GC and W10 Measurements

W10 find H21-217604 ($\alpha = 201°15733$, $\delta = -43°27402$) to have a velocity of 212 ± 10 km s^{-1}. We have two independent new velocity measurements of this object: 649 ± 18 km s^{-1} (from M2FS) and 679 ± 18 km s^{-1} (from AAOmega). The agreement between these two new measurements provides strong evidence that they are correct, and adopted the weighted average of these, excluding the W10 value.

For four additional objects, we have a new M2FS spectrum that gives a velocity inconsistent with the published one, which are discussed in detail below.

W10 find a velocity of 189 ± 34 km s^{-1} for H21-210609 ($\alpha = 201°08215$, $\delta = -42°84548$). Our M2FS velocity is 691 ± 42 km s^{-1}, with the Hβ and Mg b lines both clearly seen in the spectrum and both giving this same velocity within the uncertainties. With no specific reason to doubt our new, NGC 5128-consistent velocity, we adopt it and exclude the W10 value.

W10 find a velocity of 926 ± 44 km s^{-1} for H21-217335 ($\alpha = 201°15402$, $\delta = -43°30883$). Our M2FS velocity is 566 ± 43 km s^{-1}. Both the Hβ and Mg b lines agree with this same M2FS velocity and both are seen clearly in the good S/N spectrum. Given this agreement, we adopt the new M2FS velocity with confidence.

W10 find a velocity of 183 ± 49 km s^{-1} for H21-217458 ($\alpha = 201°15564$, $\delta = -43°10869$). Our M2FS velocity is 670 ± 55 km s^{-1}. Both the Hβ and Mg b lines agree with this same velocity, though the Mg b lines are seen more clearly than Hβ, which is weaker. Given the clear velocity from the Mg b lines, we adopt our new M2FS measurement, though with slightly lower confidence.

W10 find a velocity of 297 ± 21 km s^{-1} for H21-216619 ($\alpha = 201°14640$, $\delta = -42°96653$). Our M2FS velocity is 719 ± 73 km s^{-1}. This is a metal-poor GC and we do not get a clean velocity measurement from the Mg b lines—there is only a clear Hβ velocity. All ancillary information suggest this source is indeed a confirmed GC, and we adopt our M2FS measurement as its final velocity. However, we have the lowest confidence in this object among all of the conflicting objects, and it should be a priority for remeasurement in the future.

A.2. Resolved Conflicting Literature Measurements

We measured the velocities for four GCs listed in the table of previously classified objects with conflicting measurements from H21 (Table 6 in the Appendix of that work). Our new measurements agree with at least one of their previous measurements in the literature, and they are within the velocity range expected for GCs in NGC 5128, so we include these four GCs in Table 3 with a weighted velocity measurement that excludes the inconsistent measurement from the weighted average.

The first, H21-221818 at position $\alpha = 201°20335$, $\delta = -43°27145$, was noted as a GC by W10 with a velocity of 426 ± 41 km s^{-1} and as a background galaxy by Beasley et al. (2008) with a velocity of 42,000 km s^{-1}. We measure it to have a velocity of 440 ± 24 km s^{-1} using M2FS, confirming it to be a GC. The second, H21-257878 at position $\alpha = 201°59204$, $\delta = -43°15295$, was noted as a GC by Woodley et al. (2005) with a velocity of 505 ± 78 km s^{-1} and as a background galaxy by Beasley et al. (2008) with a velocity of 21,000 km s^{-1}. We measure it to have a velocity of 447 ± 56 km s^{-1} using AAOmega, confirming it to be a GC. The third, at position $\alpha = 201°54395$, $\delta = -43°01830$, was noted as a foreground star by Beasley et al. (2008) with a velocity of 231 ± 143 km s^{-1} and a GC by W10 with a velocity of 311 ± 81. We measure it to have a velocity of 449 ± 36 km s^{-1} using AAOmega, confirming it to be a GC (owing to the large uncertainties on the literature measurements, the conflict among the velocities here was only marginal). It did not receive an ID in H21, and we label it as H22-459 in Table 3. The fourth, H21-265571 at position $\alpha = 201°66045$, $\delta = -42°76268$, was noted as a GC with radial velocity measurements of 474 ± 65 km s^{-1} in Harris et al. (2002), 492 ± 37 km s^{-1} in Woodley et al. (2007), and 627 ± 21 km s^{-1} in W10. We measure it to have a velocity of 602 ± 15 km s^{-1} using AAOmega, confirming it to be a GC.

## A.3. Resolving Conflicting Gaia and Velocity Evidence

As noted in Section 3.3, we used a $v_r > 250$ km s^{-1} threshold for deciding on clusters being confirmed GCs based on their velocity alone. This was based at least in part on the large number of GC candidates below this velocity that turned out to be stars with highly significant ($>5\sigma$) proper motions in Gaia DR3. However, even above this velocity, there were nine new objects and four literature objects with velocities in the range 250–350 km s^{-1} and with $>5\sigma$ Gaia DR3 proper motions. The nine new objects can be found listed among the stars in Table 5. The four previous literature objects at $v_r > 250$ km s^{-1} with $>5\sigma$ proper motion detections are H21-257155 ($\alpha = 201°58596$, $\delta = -42°89608$), GC0333 ($\alpha = 201°48435$, $\delta = -43°02578$), H21-247489 ($\alpha = 201°48857$, $\delta = -43°68582$), and H21-202595 ($\alpha = 200°99837$, $\delta = -42°92202$). These can all confidently be classified as stars.

Only one object with a Gaia proper motion had a velocity >350 km s^{-1} that would be very unusual for a foreground star: Beasley et al. (2008) report the object H21-247489 ($\alpha = 201°48857$, $\delta = -43°68581$) to have a radial velocity of 601 ± 66 km s^{-1}, but this source also has a high-significance ($>5\sigma$) Gaia DR3 proper motion and does not appear extended in ground-based imaging or in Gaia. Pending an additional radial velocity measurement, we exclude this from the catalog of velocity-confirmed GCs.

On the other hand, we keep one object that has a high-significance Gaia DR3 proper motion: H21-335694 ($\alpha = 202°33212$, $\delta = -41°67356$). This object has a high S/N spectrum with all absorption lines consistent with its measured velocity at $v_r = 452$ km s^{-1} and appears extended in our ground-

based imaging. In Gaia DR3, this object shows a very high proper motion of $\mu_\alpha = -12.586 \pm 0.113$ and $\mu_\delta = -0.046 \pm 0.097$, but only in the α direction, and also has no measurable parallax, which is unusual for a high proper motion object with its G mag. We suspect the Gaia measurement may be erroneous and keep this object, pending an update of the Gaia measurement in a future data release.

ORCID iDs

Allison K. Hughes ⬤ https://orcid.org/0000-0002-1718-0402
David J. Sand ⬤ https://orcid.org/0000-0003-4102-380X
Anil Seth ⬤ https://orcid.org/0000-0003-0248-5470
Jay Strader ⬤ https://orcid.org/0000-0002-1468-9668
Chris Lidman ⬤ https://orcid.org/0000-0003-1731-0497
Karina Voggel ⬤ https://orcid.org/0000-0001-6215-0950
Antoine Dumont ⬤ https://orcid.org/0000-0003-0234-3376
Denija Crnojević ⬤ https://orcid.org/0000-0002-1763-4128
Mario Mateo ⬤ https://orcid.org/0000-0002-3856-232X
Nelson Caldwell ⬤ https://orcid.org/0000-0003-2352-3202
Duncan A. Forbes ⬤ https://orcid.org/0000-0001-5590-5518
Sarah Pearson ⬤ https://orcid.org/0000-0003-0256-5446
Puragra Guhathakurta ⬤ https://orcid.org/0000-0001-8867-4234
Elisa Toloba ⬤ https://orcid.org/0000-0001-6443-5570

References

Alabi, A. B., Forbes, D. A., Romanowsky, A. J., et al. 2017, MNRAS, 468, 3949
Alonso, M. V., & Minniti, D. 1997, ApJS, 109, 397
Baade, W., & Minkowski, R. 1954, ApJ, 119, 215
Bahcall, J. N., & Tremaine, S. 1981, ApJ, 244, 805
Beasley, M. A., Bridges, T., Peng, E., et al. 2008, MNRAS, 386, 1443
Bertin, E. 2010, SWarp: Resampling and Co-adding FITS Images Together, Astrophysics Source Code Library, ascl:1010.068
Bertin, E., & Arnouts, S. 1996, A&AS, 117, 393
Brodie, J. P., & Strader, J. 2006, ARA&A, 44, 193
Caldwell, N., & Romanowsky, A. J. 2016, ApJ, 824, 42
Caldwell, N., Schiavon, R., Morrison, H., Rose, J. A., & Harding, P. 2011, AJ, 141, 61
Chaturvedi, A., Hilker, M., Cantiello, M., et al. 2022, A&A, 657, A93
Coccato, L., Arnaboldi, M., & Gerhard, O. 2013, MNRAS, 436, 1322
Côté, P., McLaughlin, D. E., Cohen, J. G., & Blakeslee, J. P. 2003, ApJ, 591, 850
Côté, P., McLaughlin, D. E., Hanes, D. A., et al. 2001, ApJ, 559, 828
Crnojević, D., Ferguson, A. M. N., Irwin, M. J., et al. 2013, MNRAS, 432, 832
Crnojević, D., Sand, D. J., Bennet, P., et al. 2019, ApJ, 872, 80
Crnojević, D., Sand, D. J., Caldwell, N., et al. 2014, ApJL, 795, L35
Crnojević, D., Sand, D. J., Spekkens, K., et al. 2016, ApJ, 823, 19
Crockett, R. M., Shabala, S. S., Kaviraj, S., et al. 2012, MNRAS, 421, 1603
Dumont, A., Seth, A. C., Strader, J., et al. 2022, ApJ, 929, 147
Evans, N. W., Wilkinson, M. I., Perrett, K. M., & Bridges, T. J. 2003, ApJ, 583, 752
Fahrion, K., Müller, O., Rejkuba, M., et al. 2020, A&A, 634, A53
Faifer, F. R., Forte, J. C., Norris, M. A., et al. 2011, MNRAS, 416, 155
Forbes, D. A., Alabi, A., Brodie, J. P., et al. 2017, AJ, 153, 114
Forbes, D. A., Ponman, T., & O'Sullivan, E. 2012, MNRAS, 425, 66
Gaia Collaboration, Vallenari, A., Brown, A. G. A., et al. 2022, arXiv:2208.00211
Georgiev, I. Y., Hilker, M., Puzia, T. H., Goudfrooij, P., & Baumgardt, H. 2009, MNRAS, 396, 1075
Georgiev, I. Y., Puzia, T. H., Goudfrooij, P., & Hilker, M. 2010, MNRAS, 406, 1967
Gómez, M., Geisler, D., Harris, W. E., et al. 2006, A&A, 447, 877
Gómez, M., & Woodley, K. A. 2007, ApJL, 670, L105
Graham, J. A. 1979, ApJ, 232, 60
Graham, J. A., & Phillips, M. M. 1980, ApJL, 239, L97
Harris, G. L. H., Geisler, D., Harris, H. C., & Hesser, J. E. 1992, AJ, 104, 613

Harris, G. L. H., Gómez, M., Harris, W. E., et al. 2012, AJ, 143, 84
Harris, G. L. H., Harris, W. E., & Geisler, D. 2004, AJ, 128, 723
Harris, G. L. H., Rejkuba, M., & Harris, W. E. 2010, PASA, 27, 457
Harris, H. C., Harris, G. L. H., Hesser, J. E., & MacGillivray, H. T. 1984, ApJ, 287, 185
Harris, W. E. 2001, in Saas-Fee Advanced Course 28: Star Clusters, ed. L. Labhardt & B. Binggeli (Berlin: Springer), 223
Harris, W. E., Harris, G. L. H., Barmby, P., McLaughlin, D. E., & Forbes, D. A. 2006, AJ, 132, 2187
Harris, W. E., Harris, G. L. H., Holland, S. T., & McLaughlin, D. E. 2002, AJ, 124, 1435
Harris, W. E., & Racine, R. 1979, ARA&A, 17, 241
Hesser, J. E., Harris, H. C., & Harris, G. L. H. 1986, ApJL, 303, L51
Hesser, J. E., Harris, H. C., van den Bergh, S., & Harris, G. L. H. 1984, ApJ, 276, 491
Holland, S., Côté, P., & Hesser, J. E. 1999, A&A, 348, 418
Hughes, A. K., Sand, D. J., Seth, A., et al. 2021, ApJ, 914, 16
Hui, X., Ford, H. C., Freeman, K. C., & Dopita, M. A. 1995, ApJ, 449, 592
Israel, F. P. 1998, A&ARv, 8, 237
Jordán, A., Sivakoff, G. R., McLaughlin, D. E., et al. 2007, ApJL, 671, L117
Karachentsev, I. D., Tully, R. B., Dolphin, A., et al. 2007, AJ, 133, 504
Kimmig, B., Seth, A., Ivans, I. I., et al. 2015, AJ, 149, 53
Kirihara, T., Miki, Y., & Mori, M. 2017, MNRAS, 469, 3390
Kraft, R. P., Vázquez, S. E., Forman, W. R., et al. 2003, ApJ, 592, 129
Landsman, W. B. 1993, in ASP Conf. Ser. 52, Astronomical Data Analysis Software and Systems II, ed. R. J. Hanisch, R. J. V. Brissenden, & J. Barnes (San Francisco, CA: ASP), 246
Mackey, A. D., Ferguson, A. M. N., Huxor, A. P., et al. 2019, MNRAS, 484, 1756
Mackey, A. D., Huxor, A. P., Ferguson, A. M. N., et al. 2010, ApJL, 717, L11
Martini, P., & Ho, L. C. 2004, ApJ, 610, 233
Mateo, M., Bailey, J. I., III, Crane, J., et al. 2012, Proc. SPIE, 8446, 1686
McLaughlin, D. E., Barmby, P., Harris, W. E., Forbes, D. A., & Harris, G. L. H. 2008, MNRAS, 384, 563
Merrifield, M. R., & Kuijken, K. 1998, MNRAS, 297, 1292
Minniti, D., Alonso, M. V., Goudfrooij, P., Jablonka, P., & Meylan, G. 1996, ApJ, 467, 221
Minniti, D., Rejkuba, M., Funes, J. G., & Akiyama, S. 2004, ApJ, 600, 716
Mouhcine, M., Harris, W. E., Ibata, R., & Rejkuba, M. 2010, MNRAS, 404, 1157
Mould, J. R., Ridgewell, A., Gallagher, J. S. I., et al. 2000, ApJ, 536, 266
Müller, O., Fahrion, K., Rejkuba, M., et al. 2021, A&A, 645, A92
Müller, O., Lelli, F., Famaey, B., et al. 2022, A&A, 662, A57
Müller, O., Pawlowski, M. S., Jerjen, H., & Lelli, F. 2018, Sci, 359, 534
Nidever, D. L., Dey, A., Olsen, K., et al. 2018, AJ, 156, 131
Pearson, S., Price-Whelan, A. M., Hogg, D. W., et al. 2022, ApJ, 941, 19
Peng, E. W., Ford, H. C., & Freeman, K. C. 2004a, ApJS, 150, 367
Peng, E. W., Ford, H. C., & Freeman, K. C. 2004b, ApJ, 602, 705
Peng, E. W., Ford, H. C., & Freeman, K. C. 2004c, ApJ, 602, 685
Peng, E. W., Ford, H. C., Freeman, K. C., & White, R. L. 2002, AJ, 124, 3144
Pota, V., Napolitano, N. R., Hilker, M., et al. 2018, MNRAS, 481, 1744
Pryor, C., & Meylan, G. 1993, in ASP Conf. Ser. 50, Structure and Dynamics of Globular Clusters, ed. S. G. Djorgovski & G. Meylan (San Francisco, CA: ASP), 357
Rejkuba, M. 2001, A&A, 369, 812
Rejkuba, M., Dubath, P., Minniti, D., & Meylan, G. 2007, A&A, 469, 147
Rejkuba, M., Minniti, D., Courbin, F., & Silva, D. R. 2002, ApJ, 564, 688
Richstone, D. O., & Tremaine, S. 1986, AJ, 92, 72
Richtler, T. 2006, BASI, 34, 83
Richtler, T., Dirsch, B., Gebhardt, K., et al. 2004, AJ, 127, 2094
Romanowsky, A. J., Strader, J., Brodie, J. P., et al. 2012, ApJ, 748, 29
Schlafly, E. F., & Finkbeiner, D. P. 2011, ApJ, 737, 103
Schuberth, Y., Richtler, T., Hilker, M., et al. 2010, A&A, 513, A52
Schuberth, Y., Richtler, T., Hilker, M., et al. 2012, A&A, 544, A115
Sharp, R., Saunders, W., Smith, G., et al. 2006, Proc. SPIE, 6269, 62690G
Silge, J. D., Gebhardt, K., Bergmann, M., & Richstone, D. 2005, AJ, 130, 406
Sinnott, B., Hou, A., Anderson, R., Harris, W. E., & Woodley, K. A. 2010, AJ, 140, 2101
Strader, J., Caldwell, N., & Seth, A. C. 2011, AJ, 142, 8
Strigari, L. E., Bullock, J. S., Kaplinghat, M., et al. 2008, Natur, 454, 1096
Taylor, M. A., Puzia, T. H., Gomez, M., & Woodley, K. A. 2015, ApJ, 805, 65
Taylor, M. A., Puzia, T. H., Harris, G. L., et al. 2010, ApJ, 712, 1191
Taylor, M. A., Puzia, T. H., Muñoz, R. P., et al. 2017, MNRAS, 469, 3444
Tody, D. 1986, Proc. SPIE, 627, 733
Toloba, E., Guhathakurta, P., Romanowsky, A. J., et al. 2016, ApJ, 824, 35

Toloba, E., Lim, S., Peng, E., et al. 2018, ApJL, 856, L31
Tonry, J., & Davis, M. 1979, AJ, 84, 1511
van den Bergh, S., Hesser, J. E., & Harris, G. L. H. 1981, AJ, 86, 24
van Dokkum, P., Abraham, R., Brodie, J., et al. 2016, ApJL, 828, L6
van Dokkum, P. G. 2001, PASP, 113, 1420
Vasiliev, E., & Belokurov, V. 2020, MNRAS, 497, 4162
Veljanoski, J., Mackey, A. D., Ferguson, A. M. N., et al. 2014, MNRAS, 442, 2929
Voggel, K. T., Seth, A. C., Sand, D. J., et al. 2020, ApJ, 899, 140
Walker, M. G., Mateo, M., Olszewski, E. W., et al. 2007, ApJL, 667, L53
Walker, M. G., Olszewski, E. W., & Mateo, M. 2015, MNRAS, 448, 2717
Wang, J., Hammer, F., Rejkuba, M., Crnojević, D., & Yang, Y. 2020, MNRAS, 498, 2766

Wilkinson, A., Sharples, R. M., Fosbury, R. A. E., & Wallace, P. T. 1986, MNRAS, 218, 297
Wolf, J., Martinez, G. D., Bullock, J. S., et al. 2010, MNRAS, 406, 1220
Woodley, K. A., Gómez, M., Harris, W. E., Geisler, D., & Harris, G. L. H. 2010a, AJ, 139, 1871
Woodley, K. A., Harris, W. E., Puzia, T. H., et al. 2010b, ApJ, 708, 1335
Woodley, K. A., Harris, W. E., Beasley, M. A., et al. 2007, AJ, 134, 494
Woodley, K. A., Harris, W. E., & Harris, G. L. H. 2005, AJ, 129, 2654
Woodley, K. A., Raychaudhury, S., Kraft, R. P., et al. 2008, ApJ, 682, 199
Zepf, S. E., Beasley, M. A., Bridges, T. J., et al. 2000, AJ, 120, 2928
Zhang, H.-X., Peng, E. W., Côté, P., et al. 2015, ApJ, 802, 30